OPEN ACCESS

University of BRISTOL

Lloyd, R., Biggs, J., & Copley, A. (2019). The decade-long Machaze-Zinave aftershock sequence in the slowly straining Mozambique Rift. *Geophysical Journal International*, *217*(1), 504-531. https://doi.org/10.1093/gji/ggz033

Publisher's PDF, also known as Version of record

License (if available):
CC BY

Link to published version (if available):
10.1093/gji/ggz033

Link to publication record in Explore Bristol Research
PDF-document

This is the final published version of the article (version of record). It first appeared online via Oxford University Press at https://academic.oup.com/gji/article/217/1/504/5298869?searchresult=1. Please refer to any applicable terms of use of the publisher.

University of Bristol - Explore Bristol Research

General rights

This document is made available in accordance with publisher policies. Please cite only the published version using the reference above. Full terms of use are available:
http://www.bristol.ac.uk/pure/about/ebr-terms

Geophysical Journal International

Geophys. J. Int. (2019) **217,** 504–531
Advance Access publication 2019 January 22
GJI Geodynamics and tectonics

doi: 10.1093/gji/ggz033

The decade-long Machaze–Zinave aftershock sequence in the slowly straining Mozambique Rift

Ryan Lloyd[1], Juliet Biggs[1] and Alex Copley[2]

[1]*COMET, School of Earth Sciences, University of Bristol, Bristol BS8 1RJ, UK. E-mail: ryan.lloyd@bristol.ac.uk*
[2]*COMET, Bullard Labs, Department of Earth Sciences, University of Cambridge, Cambridge CB3 0EZ, UK*

Accepted 2019 January 20. Received 2019 January 12; in original form 2018 June 20

SUMMARY

Southern Mozambique is the southernmost expression of the continental East African Rift. Here, extension rates are low and rifting is achieved through normal faulting. Incipient rift environments provide an ideal location to investigate the role of reactivated pre-existing structures, aftershock sequences and fault interactions in rift development. In 2016 an M_w 5.6 earthquake occurred in the Zinave region of southern Mozambique, ∼10 km south-east of the M_w 7.0 2006 Machaze earthquake. We reanalyse ENVISAT InSAR observations of the Machaze earthquake, together with new Sentinel-1 Interferometric Synthetic Aperture Radar (InSAR) observations of the Zinave earthquake, and solve for uniform and distributed slip models for both events. We find that the Machaze earthquake occurred on a steeply dipping (∼75°) fault, in agreement with other studies, but that the Zinave earthquake occurred on an ∼60° dipping fault. The occurrence of the Zinave earthquake at the same depth as afterslip following the Machaze earthquake suggests laterally heterogeneous crustal frictional properties. The Machaze earthquake caused a Coulomb stress increase of ∼0.2 MPa on the Zinave fault. The full >10 yr record of seismicity following the Machaze event can be fit by the Omori law, showing that the Zinave earthquake is part of a decade-long aftershock sequence, consistent with long-duration aftershock sequences in other slowly straining regions. Aftershocks represent a major hazard that needs to be considered if a large earthquake were to occur in the southern East African Rift system today.

Key words: Earthquakes; Fault slip; Aftershocks; Rifts; Tectonics; Mozambique.

1 INTRODUCTION AND BACKGROUND

The continental East African Rift System (EARS) is the surface expression of the separation of the Nubian and Somalian tectonic plates. It can be followed southwards from Ethiopia to Malawi, south of which extension rates are low (<2 mm yr^{-1}; Stamps *et al.* 2008; Saria *et al.* 2014), and the focus of extension is less distinct (Chorowicz 2005; Bird *et al.* 2006). In the south of Malawi two branches of the EARS have been hypothesized based on the distribution of seismicity and faulting. These two branches are (i) the Luangwa Rift, trending northeast–southwest through Zimbabwe and Botswana (e.g. Scholz *et al.* 1976; Modisi 2000; Kinabo *et al.* 2007), and (ii) the Mozambique Rift, which continues southwards (e.g. Fairhead & Henderson 1977; Fonseca *et al.* 2014; Domingues *et al.* 2016; Stamps *et al.* 2018; Fig. 1a). Faulting in the Mozambique Rift may therefore represent the southernmost and least mature portion of the continental EARS. A band of seismicity, whose trend mirrors that of the Neoproterozoic Mozambique Mobile Belt and Karoo age tectonic structures, occurs from the Cainozoic Urema Graben in the north to the Machaze district (administrative region between 22.2° and 21.4°S, bounded in the south by the Save River) of southern Mozambique (Forster 1975; Fonseca *et al.* 2014; Fig. 1a). In the south of the Machaze district, there is little moderate or high magnitude seismicity ($>M_w$3) recorded in the USGS catalogue, possibly suggesting a change in strain rate or crustal rheology. Understanding how and where the EARS extends through this region is important for understanding the development of continental rifts.

In rift environments, pre-existing structures exhibit a control on the distribution of faulting (e.g. Milani & Davison 1988; Versfelt & Rosendahl 1989; Kinabo *et al.* 2008; Muirhead & Kattenhorn 2018). This is because the frictional strength of faults, that is, the differential stress required for slip on pre-existing faults, can be lower than the stress required for fault formation (Scholz 2002). Faults therefore represent planes of weakness and may be reactivated in stress conditions that are not orientated optimally for failure. This phenomenon has implications for incipient rifting, as large pre-existing structures can control the stress distribution and geometry of a rift (e.g. Versfelt & Rosendahl 1989; Kinabo *et al.*

© The Author(s) 2019. Published by Oxford University Press on behalf of The Royal Astronomical Society. This is an Open Access article distributed under the terms of the Creative Commons Attribution License (http://creativecommons.org/licenses/by/4.0/), which permits unrestricted reuse, distribution, and reproduction in any medium, provided the original work is properly cited.

Downloaded from https://academic.oup.com/gji/article-abstract/217/1/504/5298869 by University of Bristol Library user on 07 March 2019

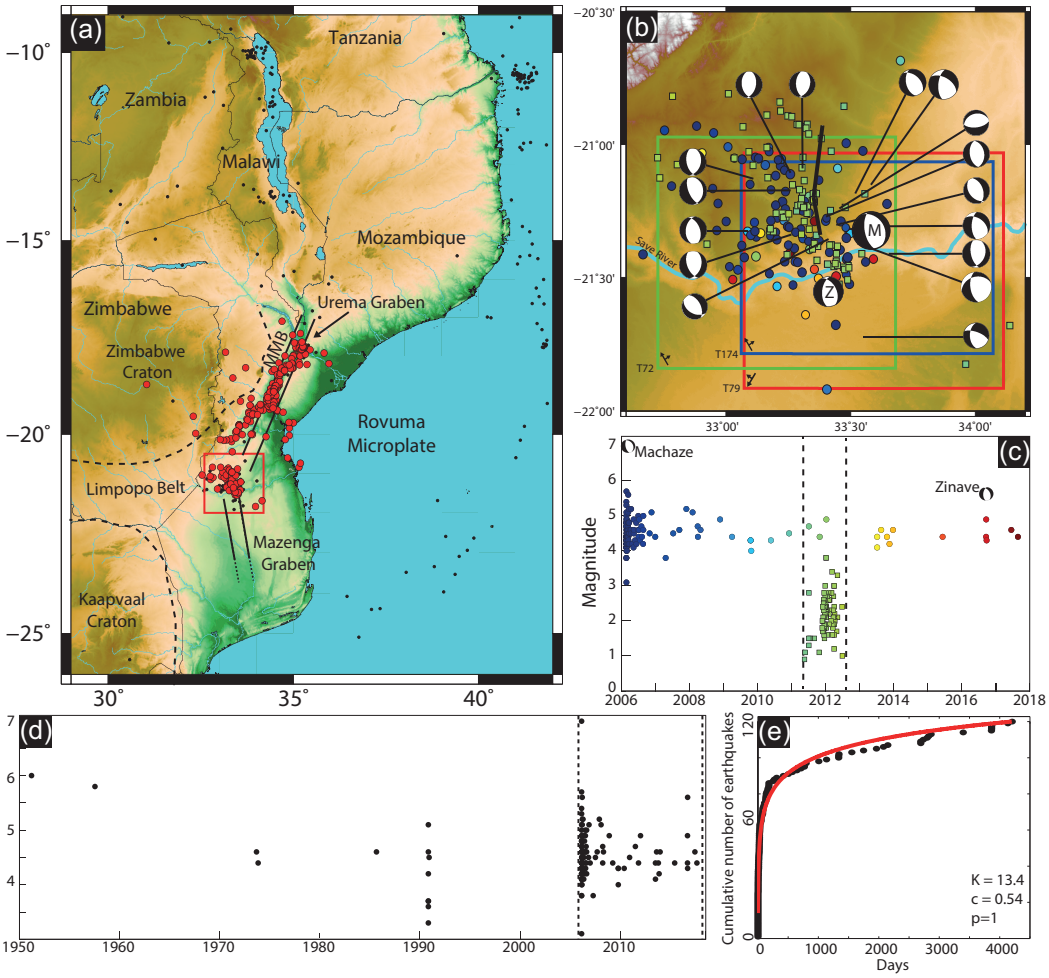

Figure 1. (a) The southern East African Rift. The red box denotes the extent of subpanel (b). The black circles show seismicity greater than magnitude 4.5 from the USGS catalogue, the red circles represent earthquakes from the MOZART catalogue (2011–2013; Fonseca *et al.* 2014). Indications of the approximate and simplified locations of the Kaapvaal and Zimbabwe Cratons, Limpopo Belt, Lebombo Dykes, Urema Graben and the Mozambique Mobile Belt (MMB) are shown by the black lines (Fonseca *et al.* 2014; Reeves *et al.* 2016). (b) The red, green and blue boxes show the cropped extents of Sentinel-1 tracks T79, T72 and T174 that are used in this study, respectively. The USGS focal mechanisms for the Machaze (M) and Zinave (Z) earthquakes are shown, with the earthquakes that occurred since the Machaze event [coloured by time, see sub-panel (c) (circles show USGS solutions, squares are events observed by Fonseca *et al.* (2014)]. The black line shows the location of the Machaze fault from Copley *et al.* (2012). (c) Magnitude–time distribution of earthquakes in the Machaze–Zinave region. The dashed lines denote the observation period of Fonseca *et al.* (2014). (d) Seismicity from 1950–2018 (USGS catalogue) showing a clear change in the rate of seismicity before and after 2006. The dashed region covers the same time period as on (c). (e) Cumulative number of earthquakes (black circles) between the Machaze and Zinave earthquakes (USGS catalogue). The red line shows the Omori law fit, with $K = 13.4$, $c = 0.54$ and $p = 1$.

2008). In some regions, however, pre-existing structures are absent or not suitably orientated for reactivation. In these cases, extension will not be fully accommodated through fault reactivation and new structures may form.

Coseismic slip induces stresses on the surrounding rock (King *et al.* 1994; Stein *et al.* 1994) that can promote or inhibit failure, either immediately or after a period of time (Tuttle *et al.* 2002; Nostro *et al.* 2005). Indeed, fault interaction plays an important role in influencing earthquake recurrence and fault growth in extensional settings (e.g. Nicol *et al.* 2010; Hodge *et al.* 2018b). In the 2009 Karonga earthquake sequence, Malawi, each new earthquake occurred within a region of positive static stress change from the previous event. This process of segmented fault rupture allowed for the lateral transition of slip on faults over ∼40 km, while being confined to the upper ∼10 km (Biggs *et al.* 2010; Fagereng 2013).

By studying incipient rifts we can observe rift development processes in action and aim to understand the growth and interaction of faults (Scholz *et al.* 1993; Walsh *et al.* 2002; Hodge *et al.* 2018b). Understanding how faults within a system interact is important in determining the induced or reduced hazard an earthquake might represent for its vicinity (e.g. Lin & Stein 2004; Wedmore *et al.* 2017). This is especially true in regions with low strain rates, which can produce long aftershock sequences (Stein & Liu 2009), elevating the hazard for up to hundreds of years after the main shock.

1.1 The Mozambique rift

On 2006 February 22, an M_w 7.0 normal faulting earthquake occurred in the Machaze region of Mozambique, in the southern East African Rift (Fenton & Bommer 2006; Yang & Chen 2008; Copley *et al.* 2012). This normal-faulting earthquake was one of the largest earthquakes in continental Africa for a century and demonstrates that the region is subject to extensional stresses. On 2016

Downloaded from https://academic.oup.com/gji/article-abstract/217/1/504/5298869 by University of Bristol Library user on 07 March 2019

September 22, 10.5 yr after and <10 km from the Machaze earthquake, an M_w 5.6 normal faulting earthquake occurred in the Zinave National Park (USGS; http://earthquake.usgs.gov).

The Machaze–Zinave region is at or near the intersection of three major inherited structures that obliquely intersect (Fig. 1a): (i) the ∼E–W Limpopo Belt, hosting the Okavango and Limpopo Dyke Swarms (∼180 Ma and 728 ± 3–1683 ± 18 Ma; Le Gall *et al.* 2002; Jourdan *et al.* 2006), (ii) the ∼NE–SW trending Urema Graben north of Machaze (Steinbruch 2010) (iii) and the ∼NNW–SSE Mazenga Graben to the south (Fig. 1a), which runs parallel to the eastern limit of the Kaapvaal Craton (Domingues *et al.* 2016). The Kaapvaal and Zimbabwe Cratons are south-west and north-west of the Machaze region, respectively. This region of the Mozambique coastal planes is thought to have a 5–10 km thick sedimentary sequence of post-Jurassic age overlying a Precambrian crystalline basement (Gwavava *et al.* 1992; Salman & Abdula 1995).

We chose to investigate the Zinave earthquake using Interferometric Synthetic Aperture Radar (InSAR) and seismology, together with a reanalysis of InSAR for the Machaze event, to better understand the tectonics of southern Mozambique. The region is poorly instrumented and difficult to access, and so satellite geodesy provides an ideal tool to investigate faulting. In this work we investigate the spatial and temporal relationships between the 2006 Machaze and 2016 Zinave earthquakes. The temporal evolution of seismicity following the Machaze earthquake is analysed, and we conclude that the Zinave earthquake is part of an aftershock sequence.

We process ENVISAT interferograms to investigate the surface deformation of the Machaze event and three overlapping tracks of Sentinel-1 data for the Zinave earthquake. We then invert the observations of surface deformation for earthquake parameters using uniform and distributed slip models. For the Zinave earthquake, we compare the geodetic models to seismological estimates of the source parameters from an inversion of body wave waveforms. The Coulomb stress transfer following the Machaze earthquake is then calculated to investigate whether the Zinave fault was brought closer to failure following the Machaze main shock. We discuss the role that the subsurface frictional properties have in the assessment of hazard, and the style of slip that could occur in this region. We relate the occurrence of these earthquakes to fault growth, the role pre-existing structures have on controlling incipient rifting and the evolution of the East African Rift.

2 SEISMICITY IN THE MOZAMBIQUE RIFT

The Machaze earthquake occurred on an ∼N–S striking fault that dipped unusually steeply (70°–75°) to the west (Fenton & Bommer 2006; Copley *et al.* 2012; Attanayake & Fonseca 2016). The fault plane is thought to be a reactivated pre-existing structure within the crystalline basement (Yang & Chen 2008; Copley *et al.* 2012). The earthquake surface rupture was >15 km in length with up to 2 m of vertical offset (Fenton & Bommer 2006). Models based on teleseismic waveforms and ENVISAT interferograms show that coseismic slip extended down to ∼25 km depth with diminishing amplitude between 10 km and the surface (Copley *et al.* 2012). This reduction of slip is interpreted to be a result of the juxtaposition of velocity weakening (crystalline basement) and velocity strengthening (sedimentary) lithologies (Copley *et al.* 2012). The shallow slip deficit was later partially recovered post-seismically through afterslip in the upper 10 km (Copley *et al.* 2012). The control of pre-existing structures and upper-crustal rheology on slip during the earthquake cycle has been similarly observed elsewhere in the EARS (e.g. Versfelt & Rosendahl 1989; Ring 1994; Kolawole *et al.* 2018).

From 1990 to 2006 there was no moderate magnitude (e.g. >M_w 4.5) seismicity observed in the Machaze region, but between the Machaze event and 2018, 134 magnitude 3 or greater earthquakes were recorded (USGS catalogue; Figs 1b and c). Between 2011 and 2013 there was a deployment of 30 seismometers throughout southern Mozambique (Fonseca *et al.* 2014). This deployment observed persistent seismicity with 143 earthquakes greater than a magnitude 0.9 in the Machaze region, indicating that the area remained seismically active (Fig. 1).

2.1 Aftershock sequences

Static and dynamic stress changes from large earthquakes cause aftershocks, which can pose a significant seismic hazard in their own right (Wiemer *et al.* 2002; Parsons *et al.* 2008; Stein & Liu 2009). We test whether the Zinave earthquake belongs to an aftershock sequence following the Machaze earthquake or is an independent event. The empirical Omori law (Omori 1894) states that the rate of aftershocks is inversely proportional to the time since the main shock. The modified version of this relationship (such that p is not equivalent to 1) is given by eq. (1) (Utsu 1961; Dieterich 1994).

$$F(t) = K/(c+t)^p. \quad (1)$$

In the modified Omori law K and c are constants that describe the productivity and the time delay of the sequence (a function of catalogue completeness), respectively. The parameter p is related to the physical heterogeneity of the aftershock region and can be time dependent (e.g. Kisslinger & Jones 1991; Helmstetter & Shaw 2006). In our analysis, we fix p to be equal to 1 for simplicity and do not consider the effects of aftershocks of aftershocks. The Omori law fits the temporal evolution of the recorded seismicity since the Machaze earthquake well with $K = 13.4$ and $c = 0.54$ (Fig. 1e). This observation suggests that the Zinave earthquake is an aftershock that occurred 10.5 yr after the Machaze earthquake. The high c value for the sequence indicates that the seismic record is likely missing events early in the sequence, which introduces uncertainty in other model parameters and supports our use of $p = 1$.

2.2 Aftershock duration in low strain rate regions

The duration of an aftershock sequence is observed to be inversely proportional to the strain rate such that regions with low strain rates have long aftershock sequences (Stein & Liu 2009). This inverse relationship is consistent with a rate-and-state description of fault friction, where the aftershock duration (t_a) is a function of the normal stress (σ_n) and the rate of shear stressing across a fault. The rate of shear stress can be approximated using the relative velocity across a fault with a simple geometry to give eq. (2) (Savage & Burford 1973),

$$t_a = (A\sigma_n \pi w)/(\mu v), \quad (2)$$

where A is a constitutive parameter (Dieterich 1994), w is the fault width, μ is the rigidity and v is the relative velocity across the fault. Using typical values, Stein & Liu (2009) determine an expected aftershock duration (in years) of $314/v$ (for v in mm yr^{-1}). In southern Mozambique, where $v \lesssim 2$ mm yr^{-1}, we may therefore expect aftershocks, and thus an significant seismic hazard, to last up to ∼150 yr (Goda 2012; Hodge *et al.* 2015).

Downloaded from https://academic.oup.com/gji/article-abstract/217/1/504/5298869 by University of Bristol Library user on 07 March 2019

3 2016 ZINAVE EARTHQUAKE

The 2016 September 22 M_w 5.6 Zinave earthquake occurred at 20:06:11 UTC. We use observations of teleseismic body waves and the surface deformation from InSAR to investigate the fault geometry and earthquake kinematics. We invert the InSAR data for coseismic uniform and distributed slip models.

3.1 Body wave inversion

We jointly inverted *P* and *SH* waveforms to obtain the strike, dip, rake, centroid depth and source time function of the Zinave event. Seismograms recorded at epicentral distances of 30°–80° were bandpass filtered at 15–100 s. These measures remove complexities due to lithospheric reverberations, interactions with the core and short-wavelength complexity in the source process or velocity structure. We can then model the earthquake as a point source, using the MT5 program of Zwick *et al.* (1994) (based on the algorithm of McCaffrey *et al.* 1991 and McCaffrey & Abers 1988). This procedure is now routine and its application in Africa is described in detail in Craig *et al.* (2011). *P* waveforms were weighted 2:1 against the *SH* waveforms to account for their lower amplitudes, and all seismograms were weighted according to azimuthal coverage. The velocity structure at the source was specified as a simple half-space velocity model, with $V_p = 3.9\,\mathrm{km\,s^{-1}}$ and $V_s = 2.2\,\mathrm{km\,s^{-1}}$, which is based on the crustal parameters used in the InSAR inversions (Section 3.3). The velocity model is relatively slow to reflect the thick sedimentary deposits.

Our best-fitting model is shown in Fig. 2. Body wave modelling indicates that, if the causative fault dipped west (as implied by the InSAR analysis below), then the earthquake occurred on a 175° striking normal fault, with a dip of 66°, rake of −69°, depth of 7 km and moment of 9.5×10^{16} Nm. The seismic estimate of the strike of this earthquake is comparable to estimates of the Machaze earthquake (175°; Yang & Chen 2008; 172° CMT), but the dip is ∼10° shallower. The resolution of the model is hampered by the lack of clear waveforms at stations in the Atlantic and Indian oceans and in Antarctica. The errors in our parameters for this event are typical for this technique and are strike ±10°, dip ±5°, rake ±10° and centroid depth ±4 km.

3.2 Sentinel-1 InSAR

To investigate the surface deformation associated with the Zinave earthquake we produced 79 Sentinel-1 interferograms, 34 of which are coseismic, from three tracks (Table A1). Interferograms were processed using the GAMMA software (Werner *et al.* 2000) within the LiCSAR facility (González *et al.* 2016). We used the 30 m SRTM DEM (Farr & Kobrick 2000) to remove topographic phase contributions and down-sampled interferograms to a 100 m final pixel size. Each interferogram was filtered using a power-law filter (strength 0.85; Goldstein & Werner 1998) and pixels with coherence values less than 0.8 were masked out.

In tropical regions, atmospheric water vapour can cause artefacts in interferograms, particularly in regions of high topography (e.g. Webley *et al.* 2004; Ebmeier *et al.* 2013; Parker *et al.* 2015). We see signs of turbulent atmospheric delays in some interferograms and test using the high-resolution European Centre for Medium-Range Weather Forecasts (HRES ECMWF) weather model through the GACOS facility to correct for them (Yu *et al.* 2017b,a). However, the model was unable to account for the observed delays with the corrections increasing the standard deviation in our data (Fig. A1). Weather models are best suited to predicting the stratified component of atmospheric delays often related to topography. In this region of southern Mozambique there is a maximum of ∼100 m elevation change over ∼100 km^2. As such, we do not expect topography-controlled atmospheric delays to be a large source of noise. We use a pair-wise logic approach to identify atmospheric delays and acquisitions with strong delays were removed (e.g. Massonnet & Feigl 1995; Ebmeier *et al.* 2013). To increase the signal-to-noise ratio, we stacked coseismic interferograms from each track, ensuring each acquisition contributed equally (Table A1, Fig. A2). Each stack was then de-ramped to remove long-wavelength atmospheric, orbital or ionospheric delays.

The Sentinel-1 interferograms show an approximately north–south trending, ∼20 km by ∼10 km region of up to ∼5 cm positive line-of-sight range change (away from the satellite), beside a smaller region of ∼1 cm negative line-of-sight range change to the east. The boundary between these two regions is relatively sharp, and the pattern is broadly consistent with that caused by an approximately north–south striking normal fault. All Sentinel-1 interferograms were highly coherent, except for coseismic ones in the river bed directly above the fault (Fig. A2). We suggest this loss of coherence is caused by liquefaction, a phenomenon that was extensive during the Machaze event (López-Querol *et al.* 2007). Chains of post-seismic interferograms for each track, covering up to 3 months after the earthquake, show no significant post-seismic deformation (Fig. A3).

The distribution of slip during an earthquake is never uniform (e.g. Reilinger *et al.* 2000; Simons *et al.* 2011; Sangha *et al.* 2017). However, the inversion for fault geometry with variable slip is nonlinear and computationally expensive. As such, we initially perform a nonlinear inversion for the fault geometry, with uniform slip, and then use this fixed geometry to linearly invert for the distribution of slip on the fault plane (e.g. Pedersen *et al.* 2003; Walters *et al.* 2009; Bie *et al.* 2017).

3.3 Zinave earthquake uniform slip modelling

We use the analytical solution for slip on a rectangular dislocation in an elastic half-space (Okada 1985) to model the surface displacements associated with the Zinave earthquake. We invert the observations of line-of-sight surface displacement using a Bayesian approach, incorporating the Markov chain Monte Carlo Metropolis-Hastings algorithm to explore the parameter space (Hastings 1970; Mosegaard & Tarantola 1995; González *et al.* 2015), and report posterior probability density functions for each model parameter. We assume all measurement errors are Gaussian. Each interferogram stack is subsampled prior to inversion, based on the interferogram variance, using the quad-tree approach (Jonsson *et al.* 2002). Initial conditions and bounds for the fault model parameters are given in Table A2. We use a Poisson's ratio of 0.25 and a shear modulus of 10 GPa for the crust to account for the thick sedimentary sequence.

The location of the Zinave earthquake is covered by three Sentinel-1 tracks (two ascending, tracks 72 and 174, and one descending, track 79). We perform five separate inversions using different subsets of the data to test the robustness of our solutions, and the influence of additional data sets on model parameter certainty, as each geodetic data set has different noise and sensitivity (Table A1, Fig. 3). All of our inversions are consistent with a north–south trending, westward dipping normal fault (Tables 1 and A3). To compare the results of each inversion, we calculate the standard deviation of the 2σ confidence bounds of each model parameter,

Downloaded from https://academic.oup.com/gji/article-abstract/217/1/504/5298869 by University of Bristol Library user on 07 March 2019

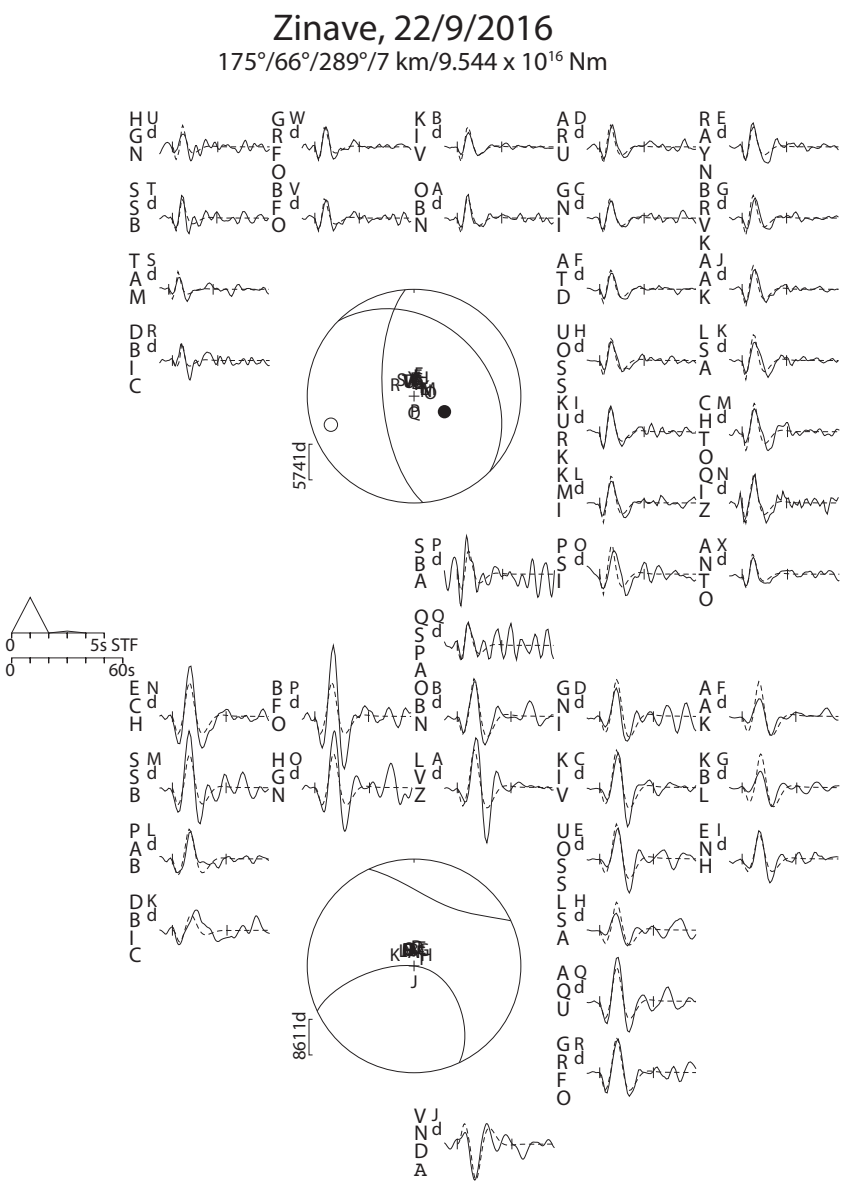

Figure 2. Focal mechanisms and source time function obtained from teleseismic body waveform modelling of (top) *P* and (bottom) *SH* waves from the Zinave earthquake. Mechanisms are shown as lower hemisphere projections. The best-fitting source parameters are strike 175°, dip 66°, rake −71° (289°), depth of 7 km and moment of 9.5 × 10^{16} Nm. Seismograms are shown as solid lines next to their station code, synthetic seismograms from the model solution are shown as dashed lines. The take-off angle for each seismogram is shown labelled on the focal sphere. The source time function (STF) is shown in the centre left.

assuming the distributions are Gaussian (Table 2). Results of inversions using individual interferograms (from T174, T79 and T72) have the largest standard deviations, indicating they are least well constrained. The overall best constrained model is that from the inversion of InSAR data from all three tracks, with between a 38 and 79 per cent decrease in the standard deviation of the parameter confidence bounds (Table 2).

The best-fitting model is for a fault that is 16 km long (95 per cent confidence: 14.8–16.7 km), with a dip of 59° (54°–67°), bottom depth 7.6 km (5.6–8.0 km) and downdip width of 5.1 km (1.4–5.7 km). All of the modelled fault parameters, 95 per cent threshold values and root-mean-square misfit values are given in Tables 1 and A3. Overall the model is able to describe the observed surface deformation well; however, there is a small residual near the southern end of the fault (Figs 4c, f and i). The spatial pattern of this residual is consistent between all of the tracks, and so is likely a feature of the rupture that is not captured by the uniform slip model.

3.4 Zinave earthquake distributed slip modelling

The model with uniform slip can reproduce the first-order patterns of surface deformation caused by the Zinave earthquake. However, systematic residuals suggest the slip was greater or shallower at the southern end of the fault. To test this, we refine our model by inverting for variable slip using the best combination of interferograms found in the previous section (stacks from ascending tracks 72 and 174, and descending track 79).

We use the plane defined in Section 3.3 (striking 168° and dipping 59°), but enlarge it to extend between the surface and a depth of

Downloaded from https://academic.oup.com/gji/article-abstract/217/1/504/5298869 by University of Bristol Library user on 07 March 2019

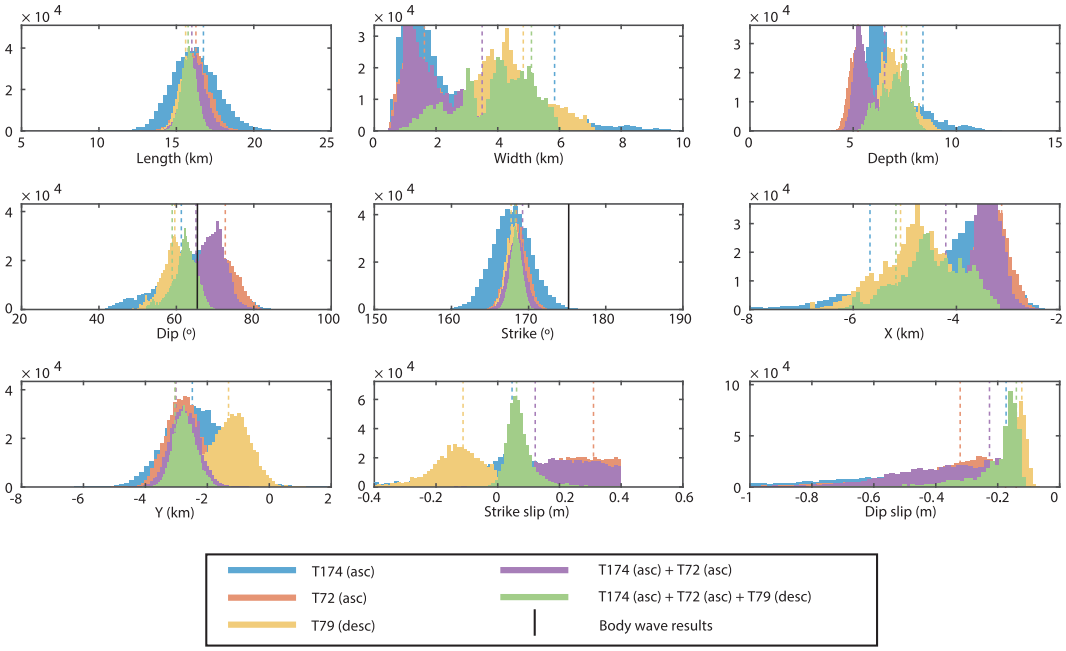

Figure 3. Marginal probability density functions for the fault parameters of the uniform slip distribution model of the Zinave earthquake. The vertical dashed lines show the optimal values from each inversion. The black vertical lines show the body wave inversion results for dip and strike (Fig. 2).

Table 1. Fault parameters from the geodetic inversions, with 95 per cent probability confidence range, and USGS focal mechanism for comparison. Fault locations [X and Y, UTM (zone 36K)] in the geodetic inversions are for the middle of the bottom of the fault. Root-mean-square (rms) misfit is the joint rms if more than one data set is used in the inversion.

Inversion points	USGS solution		T174 + T72 + T79	
	–		2071	
	FP1	FP2	Optimal	95 per cent range
Length (m)	–	–	15 800	14 900–16 800
Width (m)	–	–	5100	1400–5700
Depth (m)	15 500	15 500	7600	5600–8100
Dip (°)	45.0	50	59	54–68
Strike (°)	334	185	168	167–170
X (UTM)	550 800	550 800	546 600	545 900–548 400
Y (UTM)	7 630 800	7 630 800	7 629 300	762 900–7 632 200
Strike-slip (m)	–	–	0.06	0.0–0.20
Dip slip (m)	–	–	−0.14	−0.47– −0.12
Rake (°)	−114.0	−68.0	−66.4	–
rms (cm)	–	–	1.0	–

Table 2. Standard deviation for the marginal posterior probability density function for each parameter. The bold font indicates the smallest standard deviation for each parameter.

	T174	T72	T79	T174 + T72	T174 + T72 + T79	Decrease in standard deviation (per cent)
Length (m)	1480	830	630	710	**480**	68
Width (m)	1780	**650**	1230	770	1080	39
Depth (m)	1140	**440**	770	480	610	46
Dip (°)	7.6	4.9	3.7	4.0	**3.2**	58
Strike (°)	2.5	1.3	1.0	1.1	**0.8**	70
X (m)	990	**370**	700	**370**	620	38
Y (m)	980	550	680	460	**360**	63
Strike-slip (m)	0.18	0.09	0.08	0.09	**0.04**	79
Dip slip (m)	0.23	0.17	**0.06**	0.17	**0.06**	75

Downloaded from https://academic.oup.com/gji/article-abstract/217/1/504/5298869 by University of Bristol Library user on 07 March 2019

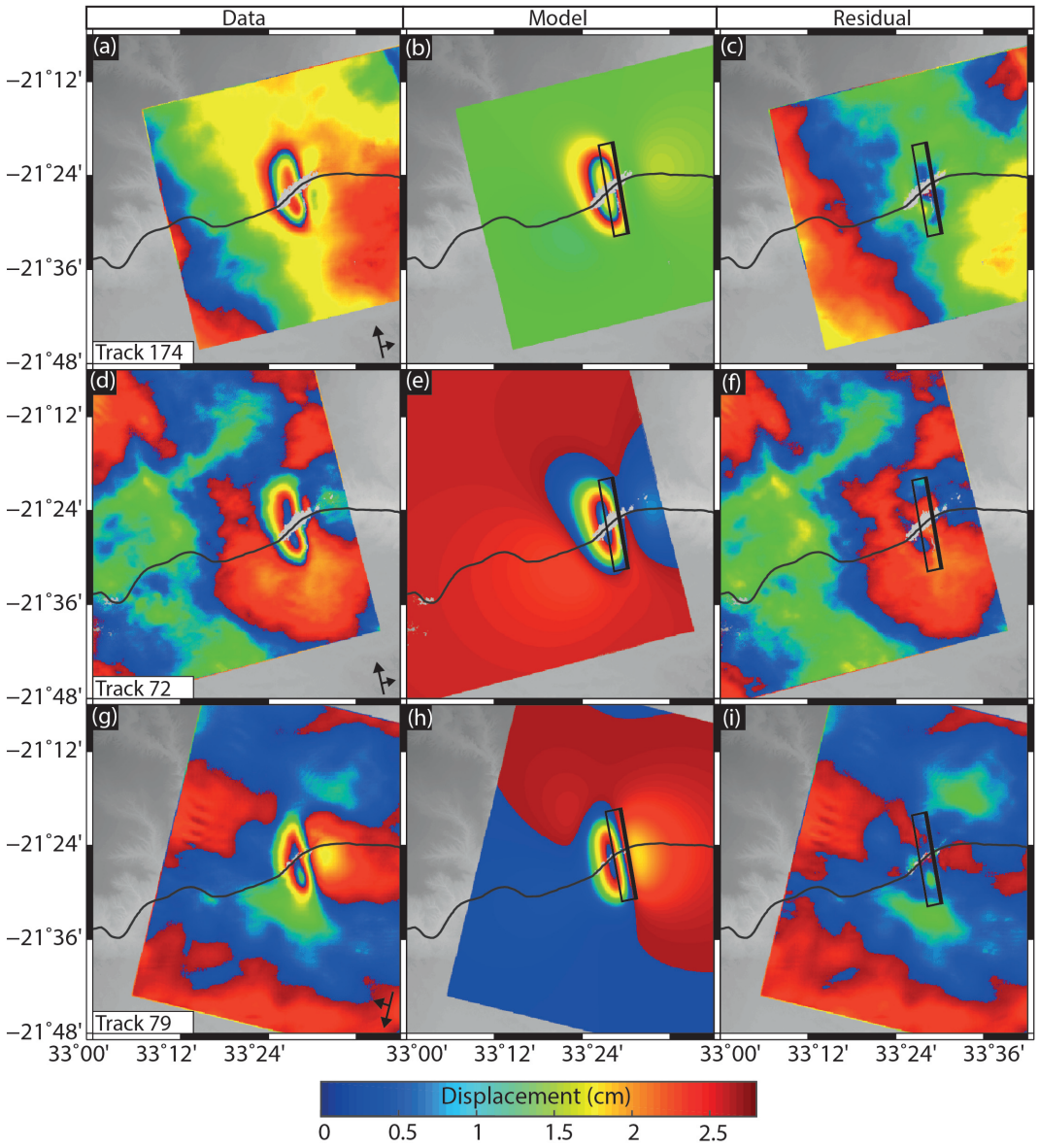

Figure 4. Data, model and residual of the uniform slip inversion for the Zinave earthquake using stacks of interferograms shown wrapped here. (a–c) Track 174, (d–f) track 72 and (h–i) track 79. The black rectangle shows the extent of the fault model and the bold line represents the up dip edge.

10 km, with a length of 24 km (Fig. 5). This plane is then divided into 100 (10 by 10) smaller patches, each of which is 2.4 km horizontal by 1 km vertical in size (see Fig. A4 for comparison to model resolution). For a fixed fault geometry, the slip on each patch can be linearly related to the observations of surface deformation (eq. 3; Wright *et al.* 2004; Funning *et al.* 2005).

$$\begin{pmatrix} \mathbf{G} & X & Y & 1 \\ \kappa^2\nabla^2 & 0 & 0 & 0 \end{pmatrix} \begin{pmatrix} \mathbf{m} \\ a \\ b \\ c \end{pmatrix} = \begin{pmatrix} \mathbf{d} \\ 0 \end{pmatrix} \tag{3}$$

Eq. (3) relates the surface displacement observation at each pixel location (described by X and Y) (**d**) to the slip on each fault patch (**m**) via the Green's function (**G**) of line-of-sight displacements from 1 m of slip on each patch, using the elastic dislocation model (Okada 1985). The formulation includes ∇^2, which is the Laplacian smoothing operator to avoid sharp slip variations (Jonsson *et al.* 2002), and κ^2 which is a prescribed scalar smoothing factor (Funning *et al.* 2005; Biggs *et al.* 2006). Eq. (3) is solved using a non-negative least-squares algorithm (Bro & De Jong 1997). In all inversions $\kappa = 5 \times 10^5$, which was selected from a trade-off curve to minimize the roughness without oversmoothing (Fig. A5a). A ramp (described by a first-order polynomial with constants a and b in the x and y directions, respectively) and an static offset (c) for each interferogram stack is also solved for in the inversion to account for long wavelength noise contributions (Biggs *et al.* 2007).

We investigate whether the rake varies across the slip region by performing three inversions: one with variable rake (**G** is formulated such that we can solve for variable rake, that is, non-negative slip in orthogonal components, between −45° and −135°, separately for each patch), one with the rake fixed from the geodetic uniform slip distribution model (−66°), and one with a rake fixed to the body wave inversion result (−71°, Fig. A6). We then compare the fit of the variable rake model considering the increase in model parameters using an F-test.

Downloaded from https://academic.oup.com/gji/article-abstract/217/1/504/5298869 by University of Bristol Library user on 07 March 2019

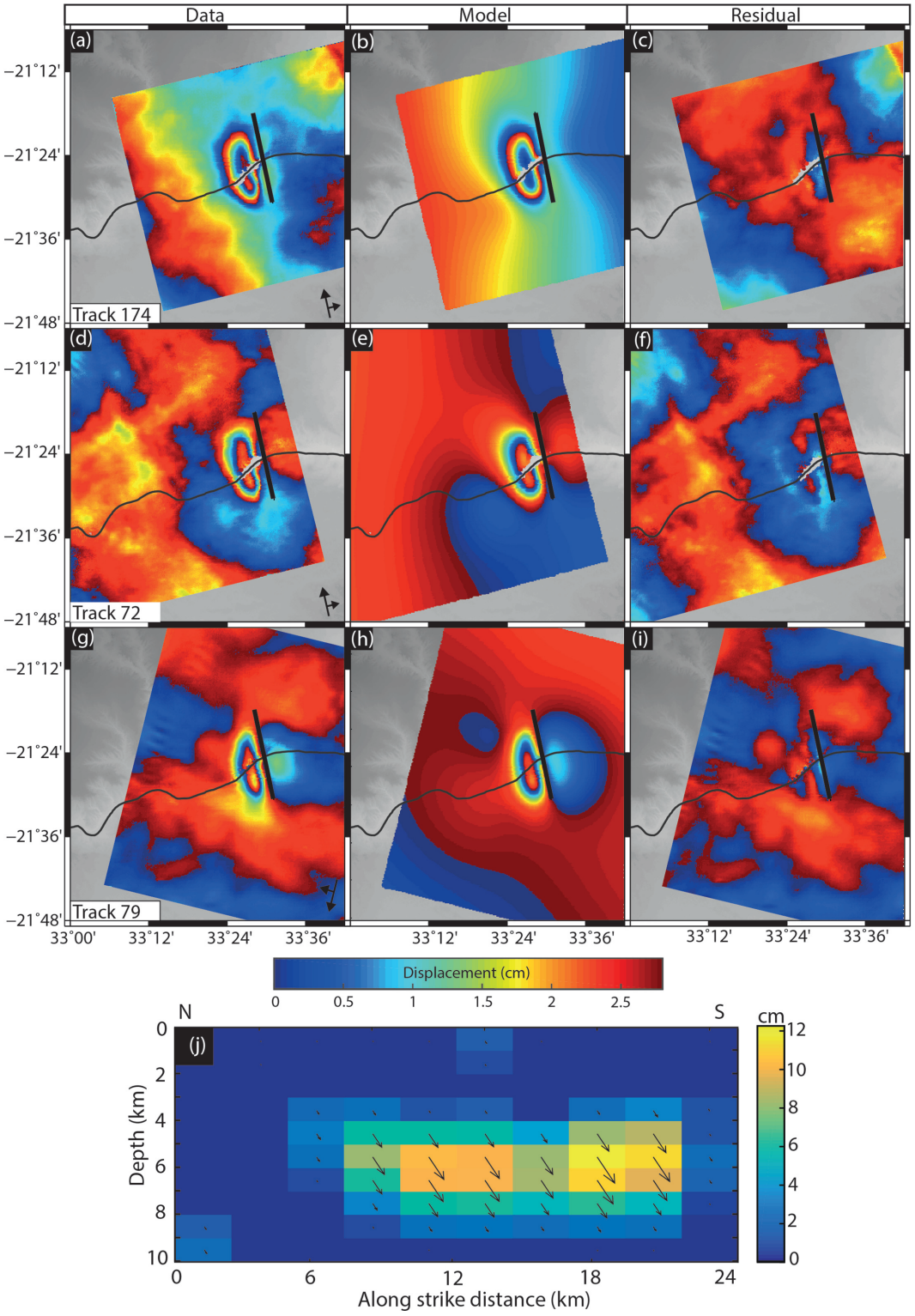

Figure 5. Distributed slip model for the Zinave earthquake. (a–c) Data, model and residual for track 174. (d–f) Track 72 data, model and residual. (g–i) Track 79 data, model and residual. The black lines a–i mark the top of the model where it intersects the surface. (j) Distributed slip model result for the inversion of tracks 174, 79 and 72 with rake fixed to –66°. The arrows show displacement of the east block relative to west (i.e. motion to the south is left-lateral).

All three inversions show no significant difference in their root-mean-square misfit (Table A4). However, in the variable rake model, the rake within the main slip region varies unrealistically, between 30° and 70° over a distance of ∼6 km (Fig. A7). A fixed rake model is a nested variant of the variable rake model (i.e. both models are described by the same equation, but the fixed rake model has fewer degrees of freedom), and as such we can perform an F-test to test whether the inclusion of variable rake is justified. The F-statistic value for this test is 0.005 considerably lower than the 5 per cent probability threshold value of 1.32. The increase in degrees of

Downloaded from https://academic.oup.com/gji/article-abstract/217/1/504/5298869 by University of Bristol Library user on 07 March 2019

freedom for the variable rake model is therefore not statistically justified and rejected.

The slip distribution for the Zinave earthquake using a fixed rake of -66°, and fit to the data are shown in Fig. 5. In comparison to the uniform slip model, there is a greater area and magnitude of slip (up to 0.12 m) at the southern end of the fault compared to the north ($\sim$0.1 m), as suggested by the residuals to the uniform slip model (Fig. 5). The region with $>$2 cm of slip is $\sim$14 km by $\sim$5 km with top and bottom boundaries at 4 km and 8 km depth, respectively. For this slip distribution, the seismic moment, using a shear modulus of 32 GPa, is 1.85×10^{17} Nm.

The geodetically and seismically derived values of dip, depth and rake for this earthquake agree within the error on both methods (Fig. 3). The seismically derived seismic moment for this event, 9.5×10^{16} Nm, is 47 per cent smaller than the geodetic estimate of the moment (1.85×10^{17} Nm). The seismic moment of an earthquake is difficult to determine accurately with both methods, and this degree of mismatch is typical (e.g. Weston *et al.* 2011).

4 2006 MACHAZE EARTHQUAKE

4.1 ENVISAT InSAR

We processed 2 ENVISAT scenes (06/06/2004 and 07/05/2006) to produce an interferogram spanning the 2006 Machaze earthquake using the ROI-PAC software (Rosen *et al.* 2004). These scenes were selected following Copley *et al.* (2012), but we remove topographic phase contributions using a 30 m DEM (Farr & Kobrick 2000), which was not available in 2012. The interferogram was filtered with strength 0.9 (Goldstein & Werner 1998). We resample the interferogram to 90 m pixel spacing and use the HRES ECMWF atmospheric model through the GACOS facility to correct for atmospheric delays in the interferogram (Yu *et al.* 2017b,a). We find that the atmospheric correction reduces the standard deviation of the interferogram from 12.1 cm (90 m pixel, no correction) to 9.6 cm (90 m pixels, atmospheric correction applied).

The use of the 30 m DEM considerably extended the connected coherent region (coherence $>$0.1) of the ENVISAT interferogram compared to the interferogram of Copley *et al.* (2012) which used a 90 m DEM, especially in the far-field and some of the signal of the fault motion. However, we were still unable to unwrap the fault within $\sim$8 km due to poor coherence and/or high deformation rate.

4.2 SPOT cross-correlation

Surface deformation can be measured using the cross-correlation of optical images (e.g. Leprince *et al.* 2007, 2008). To better constrain the near-field displacement field, we make use of two SPOT5 images, acquired on 2001 August 3 and 2008 August 26 (Copley *et al.* 2012). We use the results of Copley *et al.* (2012) who cross-correlate the images using the Cosi-Corr programme (Leprince *et al.* 2007, 2008). Due to the non-nadir viewing geometry of the satellite, vertical displacements contribute to the apparent east–west displacement (Copley *et al.* 2011). For the orientation of the Machaze earthquake and SPOT satellite viewing geometry, we calculate that the vertical displacement will destructively interfere with the east–west component. Furthermore, the subjectivity in choice of tie-points for the cross-correlation, required because of uncertain satellite orbits, reduces the reliability of the long-wavelength displacements (Copley *et al.* 2011, 2012). The displacement discontinuities, however, are robust. The acquisition dates cover both coseismic and post-seismic (30 months) periods, so the relative contribution cannot be distinguished. Nonetheless, the SPOT data set provides crucial observations of the near-field deformation (Fig. 6).

4.3 Uniform slip modelling of the Machaze earthquake using only InSAR data

In order to compare the Machaze and Zinave earthquakes, we perform inversions of observations of the Machaze earthquake using the same methodology as above. For the Machaze earthquake, we perform three inversions of the 06/06/2004–07/05/2006 ENVISAT interferogram: one with the GACOS atmospheric correction (90 m resolution; Figs 6a–c) and two without atmospheric corrections, one full resolution (30 m pixels) (Figs A8 a–c) and one resampled to 90 m (Figs A8 d–f).

We use the same inversion methodology and crustal properties as for the Zinave earthquake. Initial conditions and inversion bounds are given in Table A2. The results of all three of our inversions show that the far-field displacements captured by the ENVISAT interferograms can be well described (2.1–2.4 cm rms) by a single 24×7 km steeply dipping (78°) fault, striking 176°, with top depth $\sim$7 km below the surface (Fig. 6, 95 per cent probability values can be found in Table 3). The inversion using the interferogram with corrections for atmospheric delays is our preferred model (Table 3). The best-fitting model is a fault with 6.3 m slip at a rake of -80°. A top depth of 7 km contrasts with observations of faulting at the surface (Fenton & Bommer 2006); however, this is unsurprising as the ENVISAT data used in our inversion is incoherent close to the fault trace, resulting in little sensitivity to shallow slip. As such, we repeat the inversion including the SPOT data (Section 4.4). Our modelling results are otherwise consistent with previous seismological and geodetic estimates of the fault geometry and slip (Table 3; Copley *et al.* 2012; Fonseca *et al.* 2014).

4.4 Distributed slip modelling of the Machaze earthquake, incorporating InSAR and SPOT data

Large faults are generally complex with multiple segments (e.g. Nabelek 1985; Fletcher *et al.* 2014; Hamling *et al.* 2016). Models of the coseismic surface deformation from InSAR observations for the Machaze earthquake suggest rupture across a change in fault strike (Copley *et al.* 2012). In order to ascertain the total slip on the Machaze fault, we perform a distributed slip model with the fault location identified by displacement discontinuities in post-seismic deformation and the SPOT data (Copley *et al.* 2012). We otherwise use the same method as in Section 3.4, but with the fault divided into 3 km by 3 km patches that extends down to 30 km dipping at 75°.

We perform two inversions, (1) using just the ENVISAT interferogram ($\kappa = 7 \times 10^5$, Fig. A5b), and (2) a joint inversion using the ENVISAT interferogram and SPOT observations (which are resampled to 50 m; $\kappa = 1.3 \times 10^6$, Fig. A5c), with InSAR and SPOT data weighted equally. We solve for a ramp in the ENVISAT data and an offset in all data sets. The difference between these two models is that model 1 contains primarily far-field coseismic deformation, but omits the near-field displacement, while model 2 includes the near-field observations, but also includes 30 months post-seismic deformation. Previous observations indicate that post-seismic deformation is primarily shallow afterslip on the fault (Copley *et al.* 2012).

Downloaded from https://academic.oup.com/gji/article-abstract/217/1/504/5298869 by University of Bristol Library user on 07 March 2019

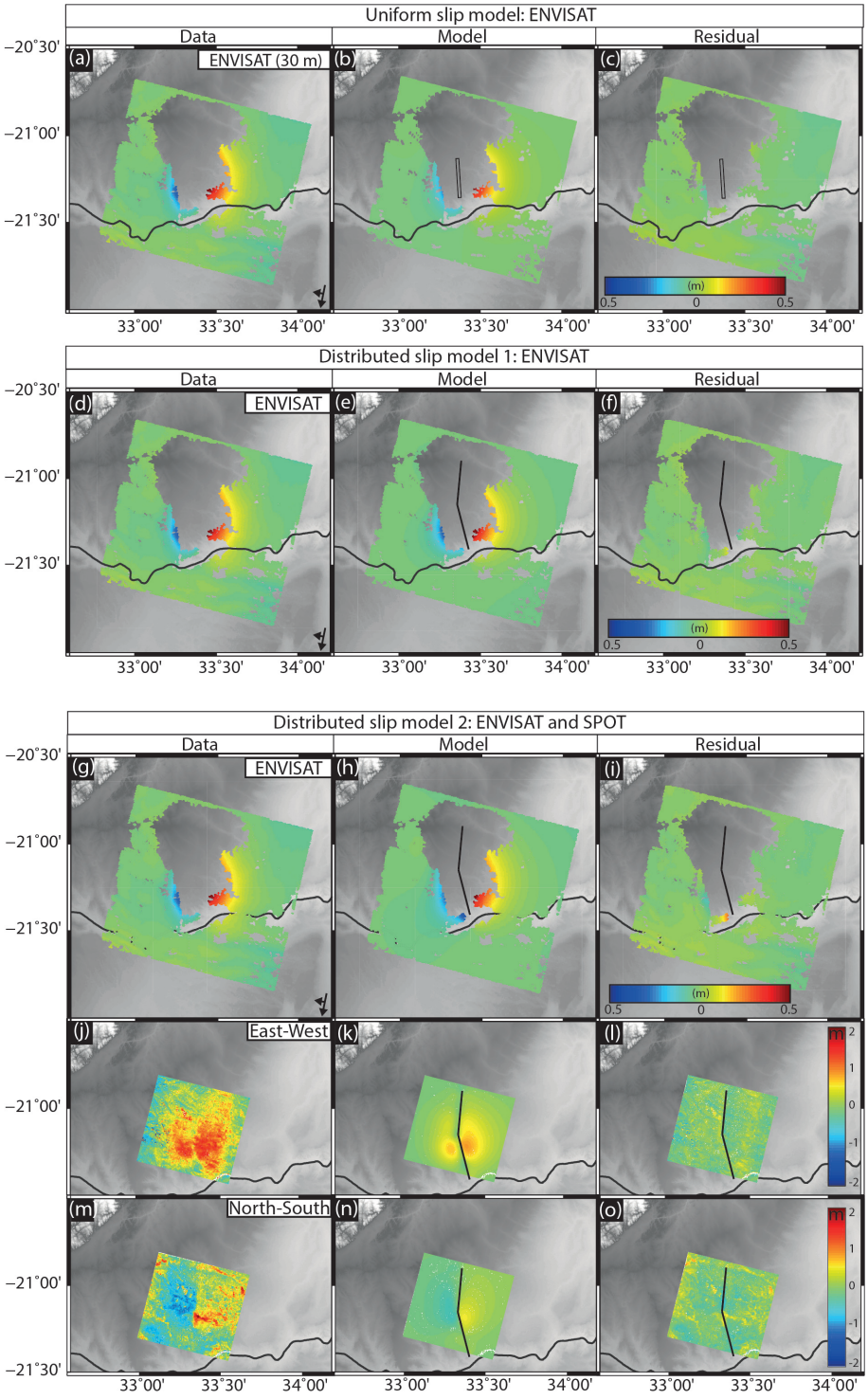

Figure 6. (a–c) Data, model and residual for the Machaze earthquake using the uniform slip model. Descending ENVISAT interferogram 06/06/2004–07/05/2006. The black rectangle on b and c shows the fault location, dipping west. (d–f) Distributed slip model 1: ENVISAT data (d), model (e), residual (f). (g–o) Distributed slip model 2, showing data, model, residual for the ENVISAT and SPOT offset data. The black line shows the modelled surface trace of the fault.

The slip distribution of model 1 indicates that the majority of the slip is concentrated towards the northern end of the southern fault, with some displacement on the northern segment (Fig. 7). The displacement is primarily normal in the main rupture area with rake values $\sim -80^{\circ}$. In this model, however, the slip in the upper cells is small, in contrast to field observations of surface offsets of up to 2 m (Fenton & Bommer 2006), probably as a result of the lack of near-field observations.

The results of the joint inversion of ENVISAT and SPOT data shows the same general pattern of slip distribution as model 1, although the slip in the uppermost cell is now 2 m (Fig. 7, resolution

Downloaded from https://academic.oup.com/gji/article-abstract/217/1/504/5298869 by University of Bristol Library user on 07 March 2019

Table 3. Model parameters and 95 per cent probability values for the Machaze earthquake inversions, and root-mean-square (RMS) misfit between the observations and the models.

	GACOS correction		No corrections		90 m no corrections	
Inversion points	1145		1186		1053	
Standard deviation (cm)	9.6		12.6131		12.11	
	Optimal	95 per cent range	Optimal	95 per cent range	Optimal	95 per cent range
Length (m)	24 500	19 300–26 400	25 800	23 000–27 500	27 100	24 800–28 500
Width (m)	6900	6500–11200	25 800	12 200–18 700	11000	10 000–14 700
Bottom depth (m)	13 700	13 400–17 400	18 400	17000–23500	16200	15 600–19 300
Dip (°)	78	75–85	76	75–82	75	74–79
Strike (°)	176	171–179	180	176–181	180	177–181
X (m)	−24 130	−24 880 – −23 200	−24 900	−25 000 – −24 000	−24 800	−25 000 – −24 200
Y (m)	8900	5200–10 600	7540	5700–8600	8100	6800–8900
Strike-slip (m)	0.96	−0.52–2.96	2.37	1.90–2.80	2.92	2.17–2.98
Dip slip (m)	−5.62	−6.00 – −3.87	−3.08	−3.47 – −2.53	−3.88	−4.20 – −2.96
Rake (°)	−80	–	−52	–	−53	–
rms (m)	0.021		0.025		0.024	

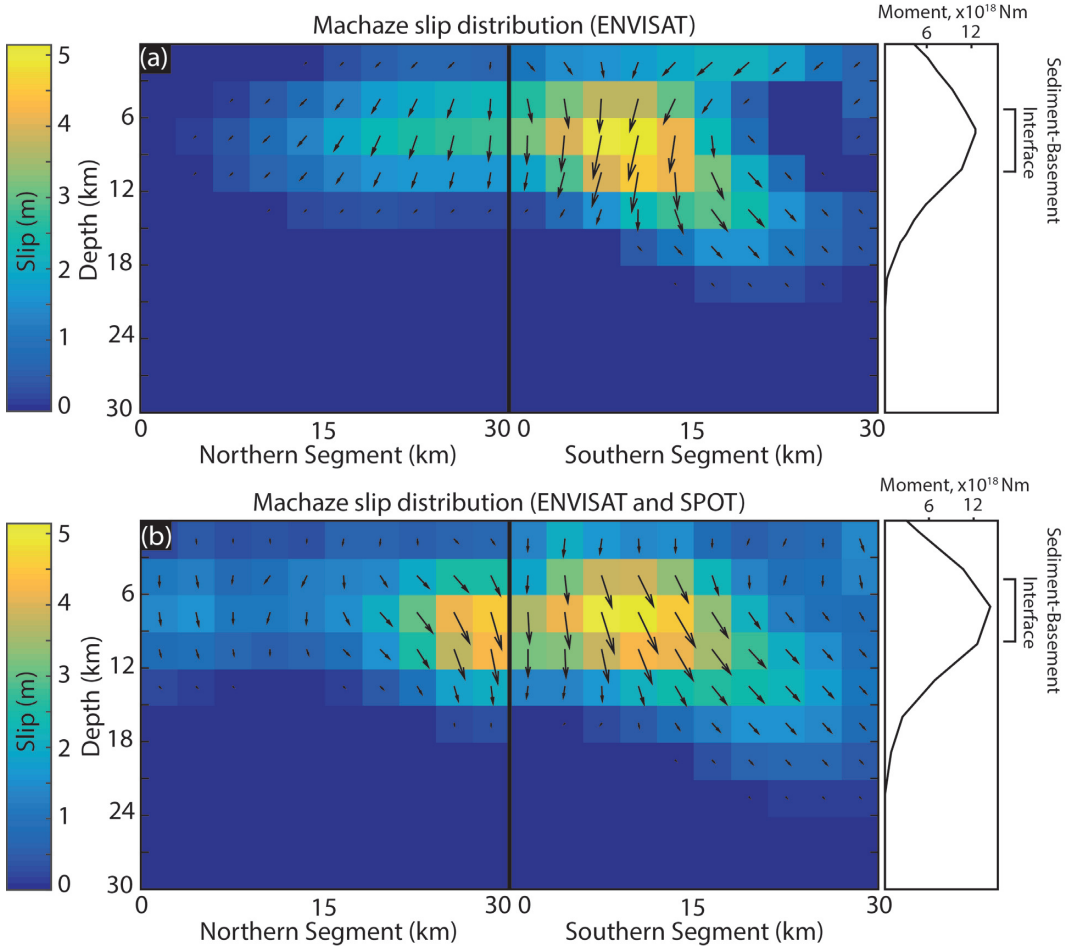

Figure 7. Slip distribution of model 1 (a, ENVISAT) and model 2 (b, ENVISAT and SPOT) for the Machaze earthquake. The estimated depth of the sediment–basement interface is shown (Salman & Abdula 1995; Gwavava *et al.* 1992). Profiles to the right of subpanels (a) and (b) show the integrated moment release with depth.

shown in Fig. A9). The slip on the southern end of the northern fault has also increased by upto 1.5 to 4.5 m. This additional slip could be either (1) post-seismic deformation, (2) coseismic deformation that is not detected by the ENVISAT interferogram due to its limited coherence or (3) an artefact, as a result of the SPOT data image-processing methodology. The greatest misfit to the data are residuals in the ENVISAT observations towards the southern end of the southern fault, where the interferogram is coherent closest to the fault trace (Fig. 6i). This may be because the SPOT data includes

Downloaded from https://academic.oup.com/gji/article-abstract/217/1/504/5298869 by University of Bristol Library user on 07 March 2019

surface deformation caused by afterslip that is modelled, but not detected by the ENVISAT observations.

Our preferred model of the coseismic slip distribution is that which is based upon the ENVISAT observations of the displacement with a fixed fault geometry based on the SPOT discontinuities (model 1). Uncertainties as to the geometry and timing (co- versus post-seismic) of the displacement in the SPOT observations introduces difficulties in how to interpret the result of model 2, although they do broadly agree with model 1, and the additional shallow slip in model 2 is consistent with post-seismic deformation.

4.5 Comparisons to seismology

The CMT and USGS estimate the coseismic moment of the Machaze earthquake to be 4.5×10^{19} and 4.6×10^{19} Nm, respectively. Using a shear modulus of 32 GPa, we calculate a seismic moment of 4.4×10^{19} Nm for our preferred model (model 1) and 5.3×10^{19} Nm for model 2. These are 5 per cent smaller and 15 per cent larger than the seismic estimates, respectively, but within the range that may be expected given the different velocity structures and possible inclusion of post-seismic deformation in the geodetic observations (Weston *et al.* 2011).

In both the geodetic distributed slip models, the majority of the moment release occurred at depths of less than 15 km (model 1: 95 per cent, model 2: 94 per cent), with a geodetic centroid of 8 km. This depth estimate is shallower than the seismological estimates of the earthquake centroid depth of 15 ± 3 km (Yang & Chen 2008), 14.8 km (Attanayake & Fonseca 2016) and 13 km (Copley *et al.* 2012). The discrepancy is likely a result of the low depth resolution in our data due to the lack of near-field geodetic observations.

The depths of Machaze aftershocks suggest that this region has a seismogenic thickness of 20 km or greater (Yang & Chen 2010; Craig *et al.* 2011). Therefore, as the Machaze earthquake ruptured down to ∼20 km, it may represent an upper bound to the size of an earthquake in this region.

4.6 Coulomb stress change

Earthquakes cause static stress changes in the surrounding rocks, bringing nearby regions closer to, or further from, failure. In theory, for failure to occur the coseismic static stress change plus any pre-existing differential stresses must be greater than a threshold Coulomb failure criterion (King *et al.* 1994; Toda *et al.* 2005). The Coulomb stress change ($\Delta\sigma_c$) is a function of the normal ($\Delta\sigma_n$) and shear stresses ($\Delta\sigma_t$) on a fault plane and is defined as

$$\Delta\sigma_c = \Delta\sigma_t + \mu' \Delta\sigma_n, \quad (4)$$

where μ' is the effective coefficient of friction that incorporates the effects of pore fluid pressure. In this formulation positive shear stress is in the direction of slip and positive normal stresses are unclamping. We use the *Coulomb 3.3* software package to calculate the $\Delta\sigma_c$ following the Machaze earthquake (Toda *et al.* 2011; Lin & Stein 2004) using slip on a rectangular dislocation model in an elastic half-space (Okada 1985). We use $\mu' = 0.4$ in our calculations and confirm that the results show little sensitivity within the range $\mu' = 0.2$–0.6.

To understand whether the Machaze earthquake could have brought the Zinave fault closer to failure, we calculate both the Coulomb and normal coseismic stress changes, and test both uniform and distributed slip models of the Machaze earthquake (Fig. 8). We calculate the Coulomb stress change at 5 km depth, comparable to that of the peak slip on the Zinave fault, and use the results from the uniform slip model for the Zinave fault to specify receiver fault geometry (Fig. 4, Table 1). Our preferred solution uses the distributed slip model based on the ENVISAT and SPOT data as it contains the most complete measure of the slip that occurred during and after the earthquake and will therefore give the best estimate of the overall stress change. Although the calculated stress changes close to the Machaze fault may be unreliable given the lack of near-field observations, they are likely to be relatively robust at distances comparable to the Machaze–Zinave separation (∼10 km). We find that the stress pattern does not vary greatly over the uncertainty range of the receiver fault parameters (strike: 166°–169°, dip: 54°–67°) given by the posterior probability density functions of our uniform slip model.

The pattern of Coulomb stress change produced by the uniform and distributed slip models of the Machaze earthquake is broadly similar. For both, at 5 km depth, the stress change is asymmetric, with the largest normal and Coulomb stress changes occurring over ∼20 km to the east (<-1 MPa) and west (>1 MPa) of the Machaze fault (Fig. 8). Lobes of positive Coulomb stress change also extend over ∼15 km to the north and south of the fault. In all models the region of the Zinave earthquake experienced a localized ∼0.2 MPa increase in Coulomb stress. This Coulomb stress change is much lower than the stress drop of the event, indicating that the fault was dominantly releasing pre-existing shear stress. Positive Coulomb stress changes are more spatially heterogeneous for the distributed slip model than the uniform slip model, with positive changes not predicted as far away from the fault to the west.

The spatial pattern of aftershocks generally follow regions of positive Coulomb stress changes (King *et al.* 1994). The distribution of recorded Machaze aftershocks (2006–2010) shows clusters in the regions of positive Coulomb stress change including near the Zinave fault (Fig. 8).

5 DISCUSSION

5.1 Rheological implications

Coseismic slip in the Machaze earthquake was largely contained within the crystalline basement, with post-seismic deformation, primarily afterslip, within the overlying sedimentary sequence. This observation led Copley *et al.* (2012) to conclude that the sediments were velocity strengthening, and the basement velocity weakening. In contrast, we find slip during the Zinave earthquake occurred primarily within the sedimentary sequence.

A transition between velocity weakening and velocity strengthening rheologies can be explained by (1) laterally variable material properties, (2) temporal variations in material properties or pore pressure or (3) stress- or time-dependent rheology. Spatial variations in frictional properties relating to lithology have been invoked to explain spatial variation in steady-state fault stability elsewhere [e.g. 2014 South Napa earthquake (Floyd *et al.* 2016) and the 2003 Tokachi-oki earthquake (Miyazaki *et al.* 2004)]. In the case of the Machaze–Zinave sequence, there are limited geological constraints on the subsurface but either depth variations in the sediment basement interface or physical variations within the sedimentary deposits are plausible. Indeed, shallow aftershocks observed by Copley *et al.* (2012) support the presence of stick-slip regions within the sedimentary sequence. In large subduction zone earthquakes aftershocks are similarly seen to concentrate in the areas dominantly

Downloaded from https://academic.oup.com/gji/article-abstract/217/1/504/5298869 by University of Bristol Library user on 07 March 2019

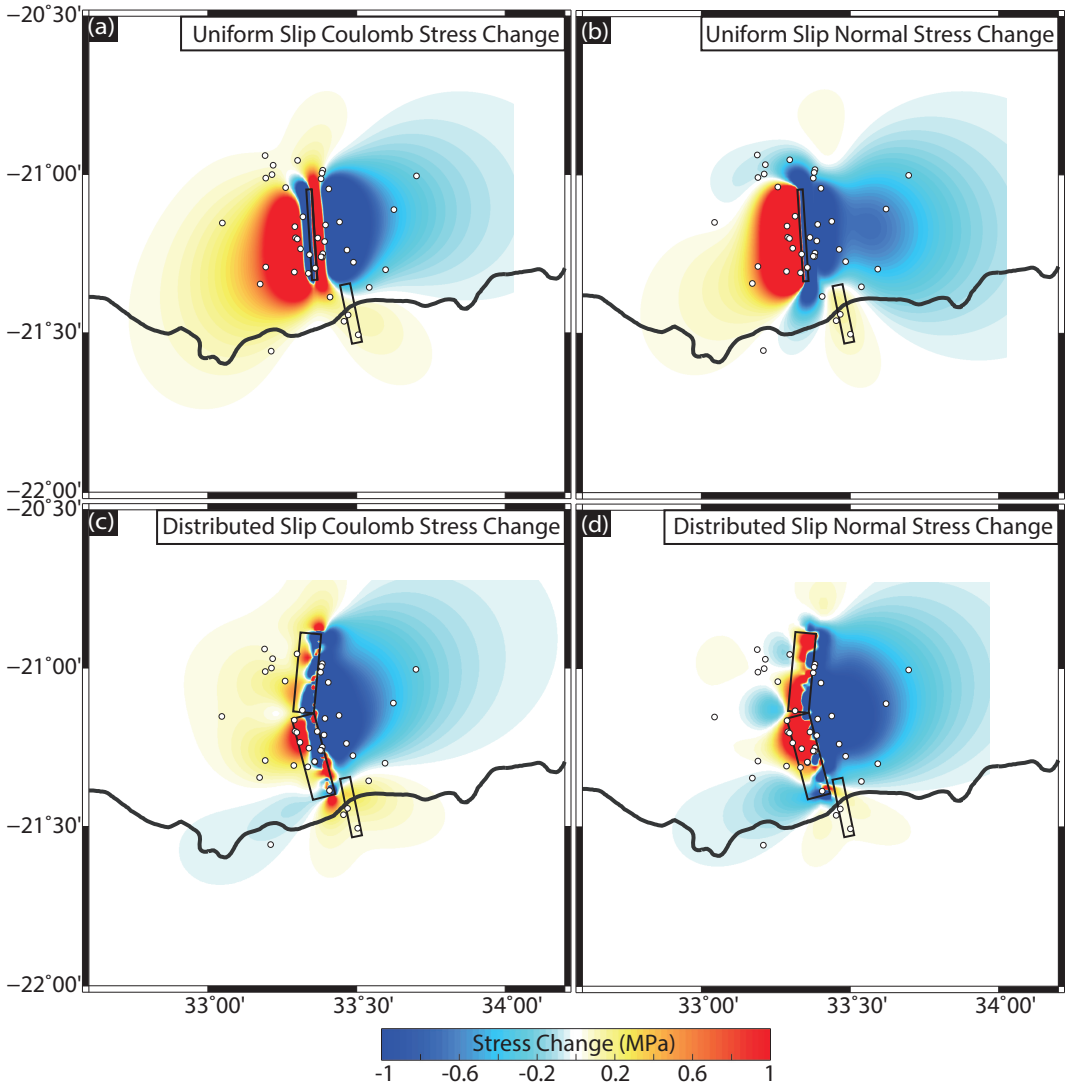

Figure 8. Coulomb stress change ($\Delta\sigma_c$) and normal stress change following the Machaze event, shown at 5 km, for receiver faults with strike 168°, dip 59° and rake −66°. (a) Coulomb stress change ($\Delta\sigma_c$) as a result of the uniform slip model of the Machaze earthquake (fault between 7 and 14 km). (b) Normal component of the stress change for the same earthquake as (a). (c) $\Delta\sigma_c$ calculated using the distributed slip model from ENVISAT and SPOT data. (d) Normal component of the $\Delta\sigma_c$ for the distributed slip model. Positive values are unclamping. The black rectangles show the vertical surface projection of the faults. The white circles show the distribution of aftershocks for all depths, 2006–2011 from Copley *et al.* (2012). See the text for further details.

deforming by aseismic creep and are generally thought to represent stuck asperities on a sliding fault surface (e.g. Igarashi *et al.* 2003; Bürgmann *et al.* 2005; Moreno *et al.* 2010).

Alternatively, temporal changes, particularly variations in pore fluid pressure, can alter the effective friction (μ') and thus control fault strength (Nur & Booker 1972; Copley 2017). This is a plausible mechanism in the Machaze region, which is a flood plain with highly seasonal rainfall, underlain by a thick sedimentary sequence of high permeability sands (López-Querol *et al.* 2007).

A steady-state, that is, rate-dependent, friction law assumes that afterslip occurs on stable faults in velocity strengthening regimes, and that the friction coefficient depends on the slip velocity only (e.g. Perfettini & Avouac 2004; Hsu *et al.* 2006). Within this framework, spatial heterogeneity would be required to explain afterslip in otherwise velocity-weakening zones. However, when the full rate-and-state law is considered, the distinction between velocity weakening and velocity strengthening is ambiguous (Helmstetter & Shaw 2009). When the steady-state constraint is not applied, fault behaviour is strongly influenced by post-seismic stresses, with both afterslip and earthquake nucleation possible within a homogenous medium.

5.2 Fault interaction and rifting

The steep dip of the Machaze earthquake fault (∼75°) and nucleation within the Precambrian basement suggests that the earthquake represents a reactivation of an existing structure, rather than the formation of a new fault (Yang & Chen 2008). The exploitation of pre-existing structures is common in nascent, and mature, rift settings (Versfelt & Rosendahl 1989; Ring 1994; Kinabo *et al.* 2008; Laó-Dávila *et al.* 2015; Domingues *et al.* 2016; Hodge *et al.* 2018a; Muirhead & Kattenhorn 2018). Pre-existing structures represent weaknesses, which, even if not optimally orientated, will fail preferentially to the formation of new faults (Scholz 2002). In contrast to

Downloaded from https://academic.oup.com/gji/article-abstract/217/1/504/5298869 by University of Bristol Library user on 07 March 2019

the Machaze earthquake, slip during the Zinave earthquake and several aftershocks (February–April 2006; Yang & Chen 2010, 2008) occurred within the post-Jurassic sedimentary layer on an ∼60° dipping plane as predicted by Andersonian mechanics.

The Machaze–Zinave sequence raises several questions about fault growth in continental rift settings. The Zinave fault could (1) act as a linking fault between horizontally offset basement structures (e.g. Hodge *et al.* 2018b) and/or (2) represent the upward continuation of faulting on pre-existing basement structures through un-faulted sediments.

Reactivation of pre-existing structures has implications for the determination of the stress field in extensional environments using earthquake slip vectors (Delvaux & Sperner 2003; Bird *et al.* 2006; Saria *et al.* 2014). If, throughout rifting, large earthquakes occur on pre-existing structures they will not fully represent the present day principle stress orientations. Similarly, however, slip during aftershocks may represent a combination of local stresses from the mainshock and regional tectonics or interseismic strain accumulation. McKenzie (1969) demonstrated that, in a triaxial stress regime, slip vectors from shallow events provide limited constraint on the orientation of the greatest principle stress.

6 CONCLUSIONS

The Zinave earthquake occurred on a 60° dipping normal fault between 4 and 8 km deep. The earthquake occurred in a region of positive Coulomb stress change associated with the 2006 Machaze event, indicating that it was brought closer to failure by the preceding earthquake. The depth of the Zinave earthquake suggests that it is contained within sedimentary deposits, at a depth co-incident with the coseismic slip deficit and post-seismic afterslip following the Machaze event. The occurrence of afterslip and aftershocks at the same depth suggests either spatially and/or temporally variable frictional properties, or that the fault exhibits time- or stress-dependent rheology.

A comparison to the modified Omori law for aftershock decay indicates that the Zinave earthquake is part of a prolonged aftershock sequence following the Machaze earthquake. Long aftershock sequences should be expected following large earthquakes in low-strain regions, suggesting that the seismic hazard in the least mature portions of the East African Rift is underestimated. The Machaze–Zinave sequence demonstrates that magnitude 4–5 earthquakes following magnitude >7 events should be expected for decades, with associated seismicity lasting for up to ∼150 yr.

ACKNOWLEDGEMENTS

RL was supported by an NERC studentship tied to the LiCS (Looking inside the Continents from Space) consortium (NE/K010956/1). JB and AC are also supported by LiCS, as well as the NERC Centre for the Observation and Modelling of Earthquakes, Volcanoes and Tectonics (COMET). JB was supported by the Natural Environment Research Council (NERC) funded RiftVolc project (NE/L013932/1, Rift volcanism: past, present and future). Atmospheric corrections were made using the Generic Atmospheric Correction Online Service for InSAR (GACOS) facility (http://ceg-research.ncl.ac.uk/v2/gacos/). The COMET Geodetic Bayesian Inversion Software (GBIS, Version 1.0) is available here: http://comet.nerc.ac.uk/gbis/. The Sentinel-1 and ENVISAT data used in this study are available through ESA. We would also like to thank Ake Fagereng, Maximilian Werner and John Elliott for useful discussions.

REFERENCES

Attanayake, J. & Fonseca, J.F., 2016. The intraplate M_w 7 Machaze earthquake in Mozambique: improved point source model, stress drop, and geodynamic implications, *J. Afr. Earth Sci.,* **117,** 252–262.

Bie, L., González, P.J. & Rietbrock, A., 2017. Slip distribution of the 2015 Lefkada earthquake and its implications for fault segmentation, *Geophys. J. Int.,* **210,** 420–427.

Biggs, J., Bergman, E., Emmerson, B., Funning, G.J., Jackson, J., Parsons, B. & Wright, T.J., 2006. Fault identification for buried strike-slip earthquakes using InSAR: the 1994 and 2004 Al Hoceima, Morocco earthquakes, *Geophys. J. Int.,* **166**(3), 1347–1362.

Biggs, J., Wright, T., Lu, Z. & Parsons, B., 2007. Multi-interferogram method for measuring interseismic deformation: Denali Fault, Alaska, *Geophys. J. Int.,* **170**(3), 1165–1179.

Biggs, J., Nissen, E., Craig, T., Jackson, J. & Robinson, D.P., 2010. Breaking up the hanging wall of a rift-border fault: the 2009 Karonga earthquakes, Malawi, *Geophys. Res. Lett.,* **37**(11), doi:10.1029/2010GL043179.

Bird, P., Ben-Avraham, Z., Schubert, G., Andreoli, M. & Viola, G., 2006. Patterns of stress and strain rate in southern Africa, *J. geophys. Res.,* **111**(8), B08402, doi:10.1029/2005JB003882.

Bro, R. & De Jong, S., 1997. A fast non-negativity-constrained least squares algorithm, *J. Chemometr.,* **11,** 393–401.

Bürgmann, R., Kogan, M.G., Steblov, G.M., Hilley, G., Levin, V.E. & Apel, E., 2005. Interseismic coupling and asperity distribution along the Kamchatka subduction zone, *J. geophys. Res.,* **110**(7), 1–17.

Chorowicz, J., 2005. The East African rift system, *J. Afr. Earth Sci.,* **43**(1-3), 379–410.

Copley, A., 2017. The strength of earthquake-generating faults, *J. geol. Soc.,* **175,** 2017–037.

Copley, A., Avouac, J.-P., Hollingsworth, J. & Leprince, S., 2011. The 2001 M_w 7.6 Bhuj earthquake, low fault friction, and the crustal support of plate driving forces in India, *J. geophys. Res.,* **116**(B8), B08405, doi:10.1029/2010JB008137.

Copley, A., Hollingsworth, J. & Bergman, E., 2012. Constraints on fault and lithosphere rheology from the coseismic slip and postseismic afterslip of the 2006 M_w 7.0 Mozambique earthquake, *J. geophys. Res.,* **117**(3), doi:10.1029/2011JB008580.

Craig, T.J., Jackson, J.A., Priestley, K. & Mckenzie, D., 2011. Earthquake distribution patterns in Africa: their relationship to variations in lithospheric and geological structure, and their rheological implications, *Geophys. J. Int.,* **185**(1), 403–434.

Delvaux, D. & Sperner, B., 2003. New aspects of tectonic stress inversion with reference to the TENSOR program, in *Geological Society, London, Special Publications,* Vol. **212,** issue 1, pp. 75–100, Geol. Soc. Publ.

Dieterich, J., 1994. A constitutive law for rate of earthquake production and its application to earthquake clustering, *J. geophys. Res.,* **99**(B2), 2601–2618.

Domingues, A., Silveira, G., Ferreira, A.M., Chang, S.J., Custodio, S. & Fonseca, J.F., 2016. Ambient noise tomography of the East African Rift in Mozambique, *Geophys. J. Int.,* **204**(3), 1565–1578.

Ebmeier, S.K., Biggs, J., Mather, T.A. & Amelung, F., 2013. Applicability of InSAR to tropical volcanoes: insights from Central America, in *Geological Society, London, Special Publications,* Vol. **380,** Issue 1, pp. 15–37, Geol. Soc. Publ.

Fagereng, Å., 2013. Fault segmentation, deep rift earthquakes and crustal rheology: insights from the 2009 Karonga sequence and seismicity in the Rukwa–Malawi rift zone, *Tectonophysics,* **601,** 216–225.

Fairhead, J. & Henderson, N., 1977. The seismicity of Southern-Africa and incipient rifting, *Tectonophysics,* **41**(4), T19–T26.

Farr, T. & Kobrick, M., 2000. Shuttle radar topography mission produces a wealth of data, *EOS Trans. Am. geophys. Un.,* **81**(48), 581–583.

Fenton, C.H. & Bommer, J.J., 2006. The M_w 7 Machaze, Mozambique, earthquake of 23 February 2006, *Seismol. Res. Lett.,* **77**(4), 426–439.

Fletcher, J.M. *et al.*, 2014. Assembly of a large earthquake from a complex fault system: surface rupture kinematics of the 4 April 2010 El Mayor Cucapah (Mexico) M_w 7.2 earthquake, *Geosphere,* **10**(4), 797–827.

Downloaded from https://academic.oup.com/gji/article-abstract/217/1/504/5298869 by University of Bristol Library user on 07 March 2019

Floyd, M.A. *et al.*, 2016. Spatial variations in fault friction related to lithology from rupture and afterslip of the 2014 South Napa, California, earthquake, *Geophys. Res. Lett.,* **43**(13), 6808–6816.

Fonseca, J.F.B.D. *et al.*, 2014. MOZART: a seismological investigation of the East African Rift in Central Mozambique, *Seismol. Res. Lett.,* **85**(1), 108–116.

Forster, R., 1975. The geological history of the sedimentary basin of Southern Mozambique, and some aspects of the origin of the Mozambique channel, *Palaeogeogr. Palaeoclimatol. Palaeoecol.,* **17,** 267–287.

Funning, G.J., Parsons, B., Wright, T.J., Jackson, J.A. & Fielding, E.J., 2005. Surface displacements and source parameters of the 2003 Bam (Iran) earthquake from Envisat advanced synthetic aperture radar imagery, *J. geophys. Res. B,* **110**(9), 1–23.

Goda, K., 2012. Nonlinear response potential of Mainshock-Aftershock sequences from Japanese earthquakes, *Bull. seism. Soc. Am.,* **102**(5), 2139–2156.

Goldstein, M.R. & Werner, L.C., 1998. Radar interferogram filtering for geophysical applications, *Geophys. Res. Lett.,* **25**(21), 4035–4038.

González, P., Walters, R., Hatton, E., Spaans, K., McDougall, A., Hooper, A. & Wright, T., 2016. LiCSAR: Tools for automated generation of Sentinel-1 frame interferograms, in *AGU Fall Meeting (Abstract G23A-1037),* San Francisco.

González, P.J., Bagnardi, M., Hooper, A.J., Larsen, Y., Marinkovic, P., Samsonov, S.V. & Wright, T.J., 2015. The 2014-2015 eruption of Fogo volcano: geodetic modeling of Sentinel-1 TOPS interferometry, *Geophys. Res. Lett.,* **42**(21), 9239–9246.

Gwavava, O., Swain, C., Podmore, F. & Fairhead, J., 1992. Evidence of crustal thinning beneath the Limpopo Belt and Lebombo monocline of southern Africa based on regional gravity studies and implications for the reconstruction of Gondwana, *Tectonophysics,* **212**(1-2), 1–20.

Hamling, I.J., Williams, C.A. & Hreinsdóttir, S., 2016. Depressurization of a hydrothermal system following the August and November 2012 Te Maari eruptions of Tongariro, New Zealand, *Geophys. Res. Lett.,* **43**(1), 168–175.

Hastings, W., 1970. Monte Carlo sampling methods using Markov chains and their applications, *Biometrika,* **57**(1), 97–109.

Helmstetter, A. & Shaw, B.E., 2006. Relation between stress heterogeneity and aftershock rate in the rate-and-state model, *J. geophys. Res.,* **111**(B7), doi:10.1029/2005JB004077.

Helmstetter, A. & Shaw, B.E., 2009. Afterslip and aftershocks in the rate-and-state friction law, *J. geophys. Res.,* **114,** doi:10.1029/2007JB005077.

Hodge, M., Biggs, J., Goda, K. & Aspinall, W., 2015. Assessing infrequent large earthquakes using geomorphology and geodesy: the Malawi Rift, *Nat. Hazards,* **76**(3), 1781–1806.

Hodge, M., Biggs, J., Fagereng, A. & Mdala, H., 2018a. Controls on early-rift geometry: new perspectives from the Bilila-Mtakataka fault, Malawi, *Geophys. Res. Lett.,* **45**(9), 3896–3905.

Hodge, M.,Fagereng & Biggs, J., 2018b. The role of coseismic Coulomb stress changes in shaping the hard link between normal fault segments, *J. geophys. Res.,* **123**(1), 797–814.

Hsu, Y.-J. *et al.*, 2006. Frictional afterslip following the 2005 Nias-Simeulue earthquake, Sumatra, *Science,* **312**(5782), 1918–1921.

Igarashi, T., Matsuzawa, T. & Hasegawa, A., 2003. Repeating earthquakes and interplate aseismic slip in the northeastern Japan subduction zone, *J. geophys. Res.,* **108**(B5), doi:10.1029/2002JB001920.

Jonsson, S., Zebker, H., Segall, P. & Amelung, F., 2002. Fault slip distribution of the 1999 M_w 7.1 Hector Mine, California, earthquake, estimated from satellite radar and GPS measurements by Sigurjo, *Bull. seism. Soc. Am.,* **92**(4), 1377–1389.

Jourdan, F., Féraud, G., Bertrand, H., Watkeys, M.K., Kampunzu, A.B. & Le Gall, B., 2006. Basement control on dyke distribution in large igneous provinces: case study of the Karoo triple junction, *Earth planet. Sci. Lett.,* **241**(1-2), 307–322.

Kinabo, B.D., Atekwana, E.A., Hogan, J.P., Modisi, M.P., Wheaton, D.D. & Kampunzu, A.B., 2007. Early structural development of the Okavango rift zone, NW Botswana, *J. Afr. Earth Sci.,* **48**(2-3), 125–136.

Kinabo, B.D., Hogan, J.P., Atekwana, E.A., Abdelsalam, M.G. & Modisi, M.P., 2008. Fault growth and propagation during incipient continental rifting: insight from a combined aeromagnetic and shuttle radar topography mission digital elevation model investigation of the Okavango Rift Zone, northwest Botswana, *Tectonics,* **27**(3), doi:10.1029/2007TC002154.

King, G. C.P., Stein, R.S. & Lin, J., 1994. Static stress changes and the triggering of earthquakes, *Int. J. Rock Mech. Min. Sci. Geomech. Abstr.,* **32**(2), A50–A51.

Kisslinger, C. & Jones, L.M., 1991. Properties of aftershock sequences in southern California, *J. geophys. Res.,* **96**(B7), 11 947–11 958.

Kolawole, F., Atekwana, E.A., Laó-Dávila, D.A., Abdelsalam, M.G., Chindandali, P.R., Salima, J. & Kalindekafe, L., 2018. Active deformation of Malawi Rift's North Basin hinge zone modulated by reactivation of pre-existing Precambrian shear zone fabric, *Tectonics,* **37**(3), 683–704.

Laó-Dávila, D.A., Al-Salmi, H.S., Abdelsalam, M.G. & Atekwana, E.A., 2015. Hierarchical segmentation of the Malawi Rift: the influence of inherited lithospheric heterogeneity and kinematics in the evolution of continental rifts, *Tectonics,* **34**(12), 2399–2417.

Le Gall, B., Tshoso, G., Jourdan, F., Féraud, G., Bertrand, H., Tiercelin, J.J., Kampunzu, A.B. & Modisi, M.P., 2002. 40Ar/39Ar geochronology and structural data from the giant Okavango and related mafic dyke swarms, Karoo Igneous province, Northern Botswana, *Earth planet. Sci. Lett.,* **202**(3-4), 595–606.

Leprince, S., Avouac, J. & Ayoub, F., 2007. Ortho-rectification, coregistration, and subpixel correlation of optical satellite and aerial images, *IEEE Trans. Geosci. Remote Sens.,* **45,** 1529–1558.

Leprince, S., Musé, P. & Avouac, J.P., 2008. In-flight CCD distortion calibration for pushbroom satellites based on subpixel correlation, *IEEE Trans. Geosci. Remote Sens.,* **46**(9), 2675–2683.

Lin, J. & Stein, R.S., 2004. Stress triggering in thrust and subduction earthquakes and stress interaction between the southern San Andreas and nearby thrust and strike-slip faults, *J. geophys. Res.,* **109**(B2), doi:10.1029/2003JB002607.

López-Querol, S., Coop, M.R., Bommer, J.J., Fenton, C. & Sim, W.W., 2007. Back-analysis of liquefaction in the 2006 Mozambique earthquake, *Georisk: Assess. Manage. Risk Eng. Syst. Geohazards,* **1**(2), 89–101.

Massonnet, D. & Feigl, K.L., 1995. Discrimination of geophysical phenomena in satellite radar interferograms, *Geophys. Res. Lett.,* **22**(12), 1537–1540.

McCaffrey, R. & Abers, G., 1988. SYN3: a program for inversion of teleseismic waveforms on microcomputers, Air Force Geophysics Laboratory Technical Report AFGL-TR-0099, Technical report, Hanscom Air Force Base, MA., *Tech. rep*.

McCaffrey, R., Zwick, P. & Abers, G., 1991. SYN4 program, *IASPEI Software Library,* **3,** 81–166.

McKenzie, D., 1969. The relationship between fault plane solutions for earthquakes and the principal stresses, *Bull. seism. Soc. Am.,* **59**(2), 591–601.

Milani, E.J. & Davison, I., 1988. Basement control and transfer tectonics in the Recôncavo-Tucano-Jatobá rift, Northeast Brazil, *Tectonophysics,* **154**(1-2), 41–70.

Miyazaki, S., Segall, P., Fukuda, J. & Kato, T., 2004. Space time distribution of afterslip following the 2003 Tokachi-oki earthquake: Implications for variations in fault zone frictional properties, *Geophys. Res. Lett.,* **31**(6), doi:10.1029/2003GL019410.

Modisi, M.P., 2000. Fault system at the southeastern boundary of the Okavango Rift, Botswana, Pergamon, *J. Afr. Earth Sci.,* **30**(3), 569–578.

Moreno, M., Rosenau, M. & Oncken, O., 2010. 2010 Maule earthquake slip correlates with pre-seismic locking of Andean subduction zone, *Nature,* **467**(7312), 198–202.

Mosegaard, K. & Tarantola, A., 1995. Monte Carlo sampling of solutions to inverse problems, *J. geophys. Res.,* **100**(B7), 12431–12447.

Muirhead, J.D. & Kattenhorn, S.A., 2018. Activation of preexisting transverse structures in an evolving magmatic rift in East Africa, *J. Struct. Geol.,* **106,** 1–18.

Nabelek, J., 1985. Geometry and mechanism of faulting of the 1980 El Asnam, Algeria, earthquake from inversion of teleseismic body waves

Downloaded from https://academic.oup.com/gji/article-abstract/217/1/504/5298869 by University of Bristol Library user on 07 March 2019

and comparison with field observations, *J. geophys. Res.,* **90**(14), 12 713–12 728.

Nicol, A., Walsh, J.J., Villamor, P., Seebeck, H. & Berryman, K.R., 2010. Normal fault interactions, paleoearthquakes and growth in an active rift, *J. Struct. Geol.,* **32**(8), 1101–1113.

Nostro, C., Chiaraluce, L., Cocco, M., Baumont, D. & Scotti, O., 2005. Coulomb stress changes caused by repeated normal faulting earthquakes during the 1997 Umbria-Marche (central Italy) seismic sequence, *J. geophys. Res.,* **110**(5), 1–19.

Nur, A. & Booker, J., 1972. Aftershocks caused by pore fluid flow?, *Science,* **175**(4024), 885–887.

Okada, Y., 1985. Surface deformation due to shear and tensile faults in a half-space, *Int. J. Rock Mech. Min. Sci. Geomech. Abstr.,* **75**(4), 1135–1154.

Omori, F., 1894. On after-shocks of earthquakes, *J. Coll. Sci. Imp. Univ. Tokyo,* **7,** 111–200.

Parker, A.L., Biggs, J., Walters, R.J., Ebmeier, S.K., Wright, T.J., Teanby, N.A. & Lu, Z., 2015. Systematic assessment of atmospheric uncertainties for InSAR data at volcanic arcs using large-scale atmospheric models: application to the Cascade volcanoes, United States, *Remote Sens. Environ.,* **170,** 102–114.

Parsons, T., Ji, C. & Kirby, E., 2008. Stress changes from the 2008 Wenchuan earthquake and increased hazard in the Sichuan basin, *Nature,* **454**(7203), 509–510.

Pedersen, R., Jónsson, S., Árnadóttir, T., Sigmundsson, F. & Feigl, K.L., 2003. Fault slip distribution of two June 2000 M_W6.5 earthquakes in South Iceland estimated from joint inversion of InSAR and GPS measurements, *Earth planet. Sci. Lett.,* **213**(3-4), 487–502.

Perfettini, H. & Avouac, J.-P., 2004. Postseismic relaxation driven by brittle creep: a possible mechanism to reconcile geodetic measurements and the decay rate of aftershocks, application to the Chi-Chi earthquake, Taiwan, *J. geophys. Res.,* **109**(B2), doi:10.1029/2003JB002488.

Reeves, C.V., Teasdale, J.P. & Mahanjane, E.S., 2016. Insight into the Eastern Margin of Africa from a new tectonic model of the Indian Ocean, in *Geological Society, London, Special Publications,* Vol. **431,** Issue 1, pp. 299–322, Geol. Soc. Publ.

Reilinger, R.E., Ergintav, S., Bürgmann, R., Segall, P., Hearn, E.H., McClusky, S., Woith, H. & Zschau, J., 2000. Time-dependent distibuted afterslip on and deep below the Izmit earthquake rupture, *Bull. seism. Soc. Am.,* **92**(1), 126–137.

Ring, U., 1994. The influence of preexisting structure on the evolution of the Cenozoic Malawi rift (East African rift system), *Tectonics,* **13**(2), 313–326.

Rosen, P.A., Hensley, S., Peltzer, G. & Simons, M., 2004. Updated repeat orbit interferometry package released, *EOS Trans. Am. Geophys. Un.,* **85**(5), 47–47.

Salman, G. & Abdula, I., 1995. Development of the Mozambique and Ruvuma sedimentary basins, offshore Mozambique, *Sedimentary Geol.,* **96,** 7–41.

Sangha, S., Peltzer, G., Zhang, A., Meng, L., Liang, C., Lundgren, P. & Fielding, E., 2017. Fault geometry of 2015, M_w 7.2 Murghab, Tajikistan earthquake controls rupture propagation: insights from InSAR and seismological data, *Earth planet. Sci. Lett.,* **462,** 132–141.

Saria, E., Calais, E., Stamps, D.S., Delvaux, D. & Hartnady, C. J.H., 2014. Present-day kinematics of the East African Rift, *J. geophys. Res.,* **119**(4), 3584–3600.

Savage, J.C. & Burford, R.O., 1973. Geodetic determination of relative plate motion in central California, *J. geophys. Res.,* **78**(5), 832–845.

Scholz, C., 2002. *The Mechanics of Earthquakes and Faulting,* 2nd edn., Cambridge University Press.

Scholz, C.H., Koczynski, T.A. & Hutchins, D.G., 1976. Evidence for incipient rifting in Southern Africa, *Geophys. J. Royal Astron. Soc.,* **44**(1), 135–144.

Scholz, C.H., Dawers, N.H., Yu, J.-Z., Anders, M.H. & Cowie, P.A., 1993. Fault growth and fault scaling laws: preliminary results, *J. geophys. Res.,* **98**(B12), 21 951–21 961.

Simons, M. *et al.*, 2011. The 2011 magnitude 9.0 Tohoku-Oki earthquake: mosaicking the megathrust from seconds to centuries, *Science,* **332**(6036), 1421–1425.

Stamps, D.S., Calais, E., Saria, E., Hartnady, C., Nocquet, J.-M., Ebinger, C.J. & Fernandes, R.M., 2008. A kinematic model for the East African Rift, *Geophys. Res. Lett.,* **35**(5), doi:10.1029/2007GL032781.

Stamps, D.S., Saria, E. & Kreemer, C., 2018. A geodetic strain rate model for the east African rift system, *Sci. Rep.,* **8**(1), 732.

Stein, R.S., King, G. C.P. & Lin, J., 1994. Stress triggering of the 1994 M = 6.7 Northridge, California, earthquake by its predecessors, *Science,* **265**(5177), 1432–1435.

Stein, S. & Liu, M., 2009. Long aftershock sequences within continents and implications for earthquake hazard assessment, *Nature,* **462**(7269), 87–89.

Steinbruch, F., 2010. Geology and geomorphology of the Urema Graben with emphasis on the evolution of Lake Urema, *J. Afr. Earth Sci.,* **58**(2), 272–284.

Toda, S., Stein, R.S., Richards-Dinger, K. & Bozkurt, S.B., 2005. Forecasting the evolution of seismicity in southern California: animations built on earthquake stress transfer, *J. geophys. Res. B,* **110**(5), 1–17.

Toda, S., Stein, R.S., Sevilgen, V. & Jian Lin, U., 2011. Coulomb 3.3 graphic-rich deformation and stress-change software for earthquake, tectonic, and volcano research and teaching - user guide, *Tech. rep.,* USGS Open File Report.

Tuttle, M.P., Schweig, E.S., Sims, J.D., Lafferty, R.H., Wolf, L.W. & Haynes, M.L., 2002. The earthquake potential of the New Madrid seismic zone, *Bull. seism. Soc. Am.,* **92**(6), 2080–2089.

Utsu, T., 1961. A statistical study on the occurence of aftershocks, *Geophys. Mag.,* **30,** 512–605.

Versfelt, J. & Rosendahl, B., 1989. Relationships between pre-rift structure and rift architecture in Lakes Tanganyika and Malawi, East Africa, *Nature,* **337**(6205), 354–357.

Walsh, J., Nicol, A. & Childs, C., 2002. An alternative model for the growth of faults, *J. Struct. Geol.,* **24**(11), 1669–1675.

Walters, R.J. *et al.*, 2009. The 2009 L'Aquila earthquake (central Italy): a source mechanism and implications for seismic hazard, *Geophys. Res. Lett.,* **36**(17), doi:10.1029/2009GL039337.

Webley, P., Wadge, G. & James, I., 2004. Determining radio wave delay by non-hydrostatic atmospheric modelling of water vapour over mountains, *Phys. Chem. Earth A/B/C,* **29**(2-3), 139–148.

Wedmore, L.N.J., Faure Walker, J.P., Roberts, G.P., Sammonds, P.R., McCaffrey, K.J.W. & Cowie, P.A., 2017. A 667 year record of coseismic and interseismic Coulomb stress changes in central Italy reveals the role of fault interaction in controlling irregular earthquake recurrence intervals, *J. geophys. Res.,* **122**(7), 5691–5711.

Werner, C., Wegmüller, U., Strozzi, T. & Wiesmann, A., 2000. *GAMMA SAR and Interferometric Processing Software*.

Weston, J., Ferreira, A.M. & Funning, G.J., 2011. Global compilation of interferometric synthetic aperture radar earthquake source models: 1. Comparisons with seismic catalogs, *J. geophys. Res.,* **116**(8), B08408, doi:10.1029/2010JB008131.

Wiemer, S., Gerstenberger, M. & Hauksson, E., 2002. Mine earthquake: implications for aftershock hazard, *Bull. seism. Soc. Am.,* **92**(4), 1227–1240.

Wright, T.J., Parsons, B.E. & Lu, Z., 2004. Toward mapping surface deformation in three dimensions using InSAR, *Geophys. Res. Lett.,* **31,** 1–5.

Yang, Z. & Chen, W.P., 2008. Mozambique earthquake sequence of 2006: high-angle normal faulting in southern Africa, *J. geophys. Res.,* **113**(12), doi:10.1029/2007JB005419.

Yang, Z. & Chen, W.P., 2010. Earthquakes along the East African Rift System: a multiscale, system-wide perspective, *J. geophys. Res.,* **115**(12), doi:10.1029/2009JB006779.

Yu, C., Li, Z. & Penna, N.T., 2017a. Interferometric synthetic aperture radar atmospheric correction using a GPS-based iterative tropospheric decomposition model, *Remote Sens. Environ.,* **204,** 109–121.

Yu, C., Penna, N.T. & Li, Z., 2017b. Generation of real-time mode high-resolution water vapor fields from GPS observations, *J. geophys. Res.,* **122**(3), 2008–2025.

Downloaded from https://academic.oup.com/gji/article-abstract/217/1/504/5298869 by University of Bristol Library user on 07 March 2019

Zwick, P., McCaffrey, R. & Abers, G., 1994. *MT5 program, IASPEI Software Library, 4*.

SUPPORTING INFORMATION

Supplementary data are available at *GJI* online.

Please note: Oxford University Press is not responsible for the content or functionality of any supporting materials supplied by the authors. Any queries (other than missing material) should be directed to the corresponding author for the article.

APPENDIX A: DISTRIBUTED SLIP MODEL RESOLUTION

The resolution matrix for the distributed slip model, **R**, is dependent on the smoothed Green's function, where $\mathbf{G}_s$ is $[\mathbf{G}\kappa^2\nabla^2]^T$ (Jonsson *et al.* 2002; Funning *et al.* 2005). The resolution matrix is given by

$$\mathbf{R} = \left(\mathbf{G}_s^T\mathbf{G}_s\right)^{-1}\mathbf{G}^T\mathbf{G}. \quad \text{(A1)}$$

The diagonal values of **R** represent the model resolution. We define the horizontal and vertical resolution length scales for each patch as the distance in each direction over which the values are greater than $1/e$ of the maximum value of the resolution matrix (Funning *et al.* 2005; Biggs *et al.* 2006). For perfectly resolved models **R** will be an identity matrix. The distributed slip model for the Zinave earthquake has 7.5 and 5 km horizontal and vertical resolutions in the peak slip region, respectively (Fig. A4). The inversion for the slip distribution of the Machaze earthquake using ENVISAT data (model 1) has a more variable resolution, but is ∼14 km in the horizontal and vertical in the peak slip region (Fig. A8).

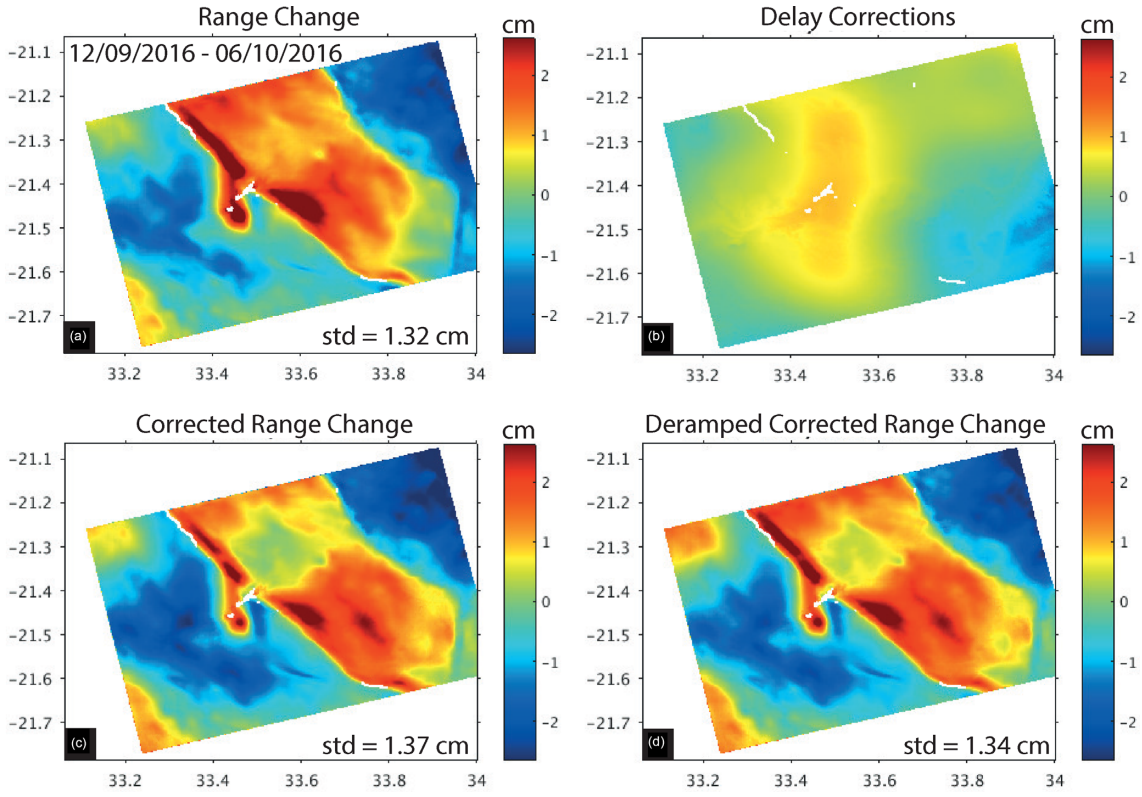

Figure A1. Atmospheric corrections for Zinave coseismic interferogram 12/09/2016–06/10/2016 (track 174). (a) Observations, (b) delay correction, (c) corrected observations, (d) de-ramped corrected observations. Standard deviations (std) for (a), (b) and (d) are shown.

Downloaded from https://academic.oup.com/gji/article-abstract/217/1/504/5298869 by University of Bristol Library user on 07 March 2019

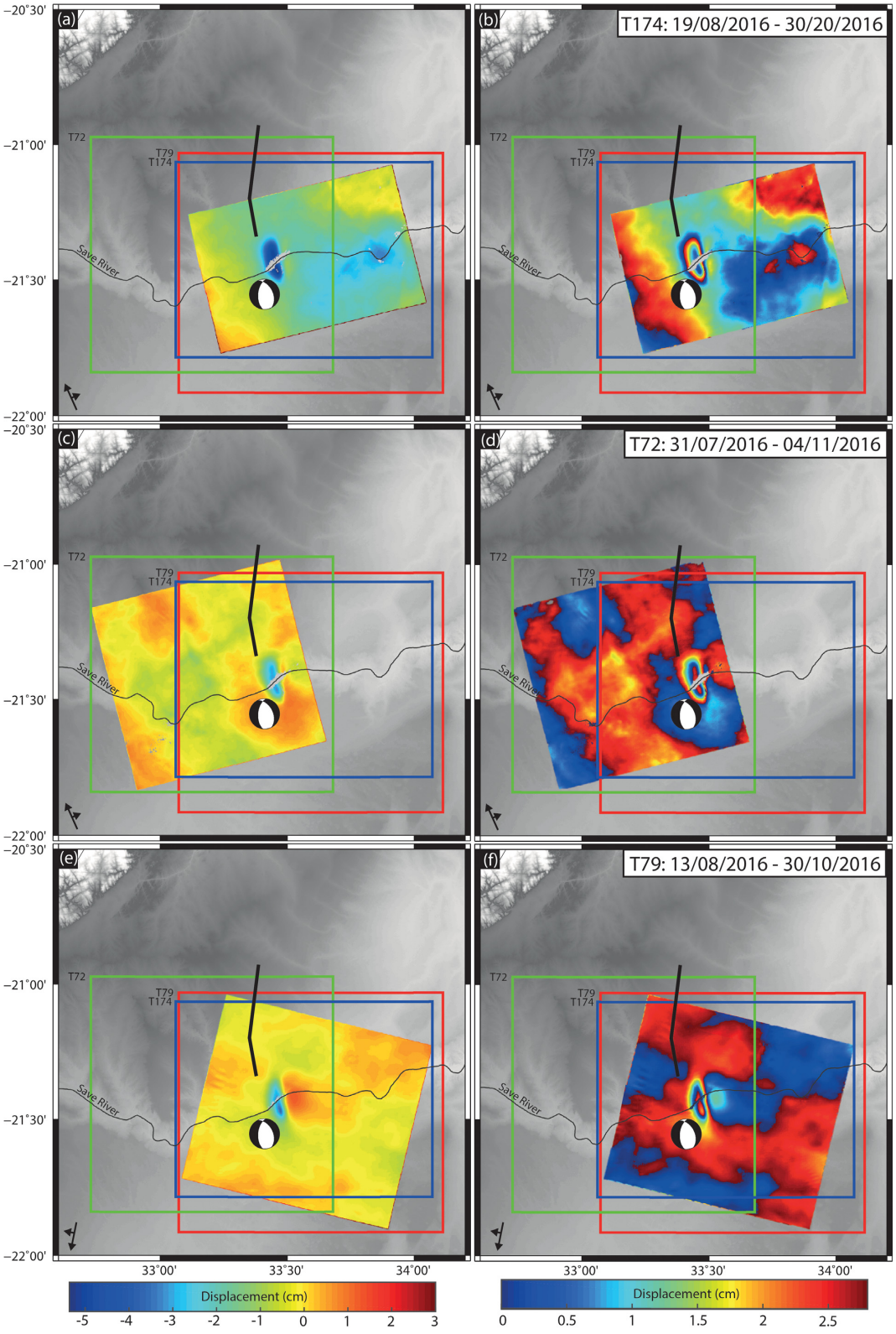

Figure A2. Unwrapped (left-hand column) and wrapped (right-hand column) stacked Sentinel-1 interferograms of the Zinave earthquake from tracks T174 (top), T72 (middle) and T79 (bottom). The black line shows the location of the Machaze earthquake fault from Copley *et al.* (2012).

Downloaded from https://academic.oup.com/gji/article-abstract/217/1/504/5298869 by University of Bristol Library user on 07 March 2019

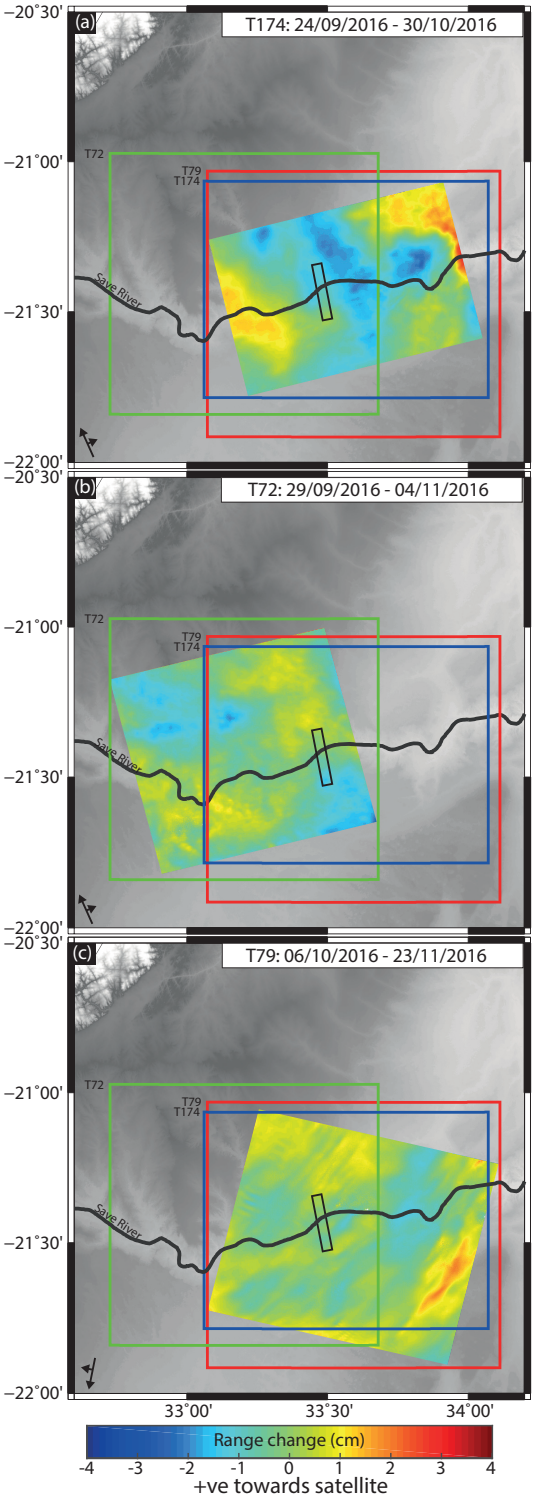

Figure A3. Observations of the post-seismic range change following the Zinave earthquake for (a) track 174: 24/09/2016–30/10/2016, (b) track 72: 29/09/2016–04/11/2016, (c) track 79 06/10/2016–23/11/2016, showing no deformation.

Downloaded from https://academic.oup.com/gji/article-abstract/217/1/504/5298869 by University of Bristol Library user on 07 March 2019

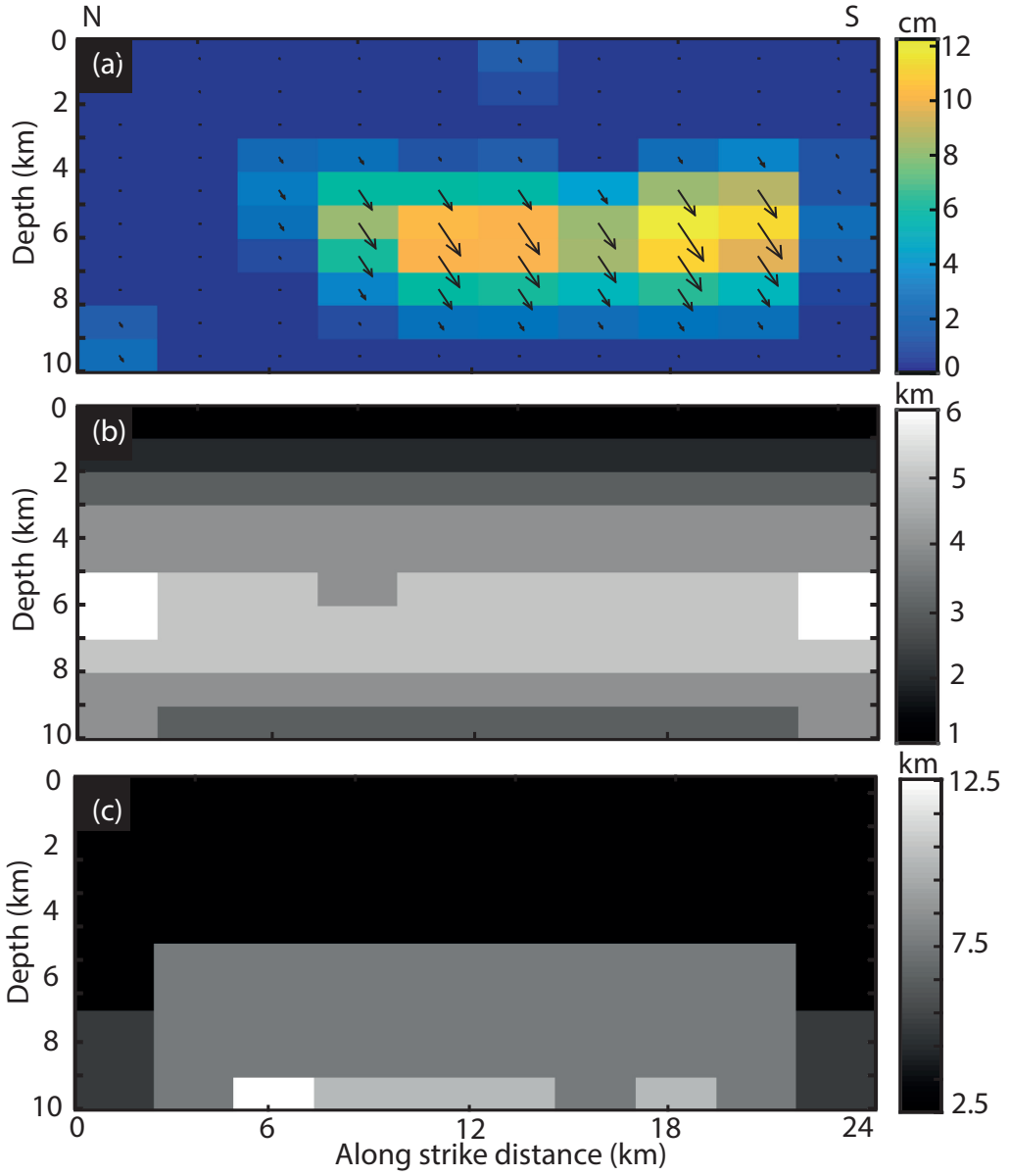

Figure A4. (a) Slip distribution for the Zinave earthquake with rake fixed at −66°. (b) Length scale of vertical resolution. (c) Length scale of horizontal resolution. Each cell is 1 km horizontally by 2.4 km vertically.

Downloaded from https://academic.oup.com/gji/article-abstract/217/1/504/5298869 by University of Bristol Library user on 07 March 2019

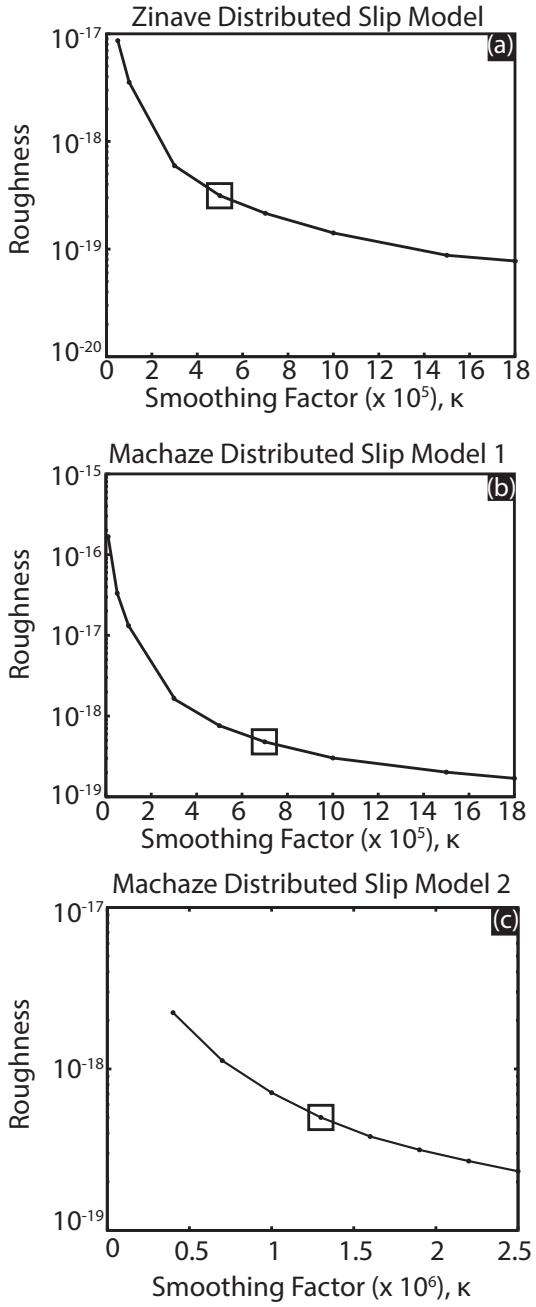

Figure A5. Smoothing factor versus model roughness for (a) Zinave distributed slip model, (b) Machaze model 1 (ENVISAT), (c) Machaze model 2 (ENVISAT and SPOT). The chosen smoothing factor value is shown by a black box in each subplot.

Downloaded from https://academic.oup.com/gji/article-abstract/217/1/504/5298869 by University of Bristol Library user on 07 March 2019

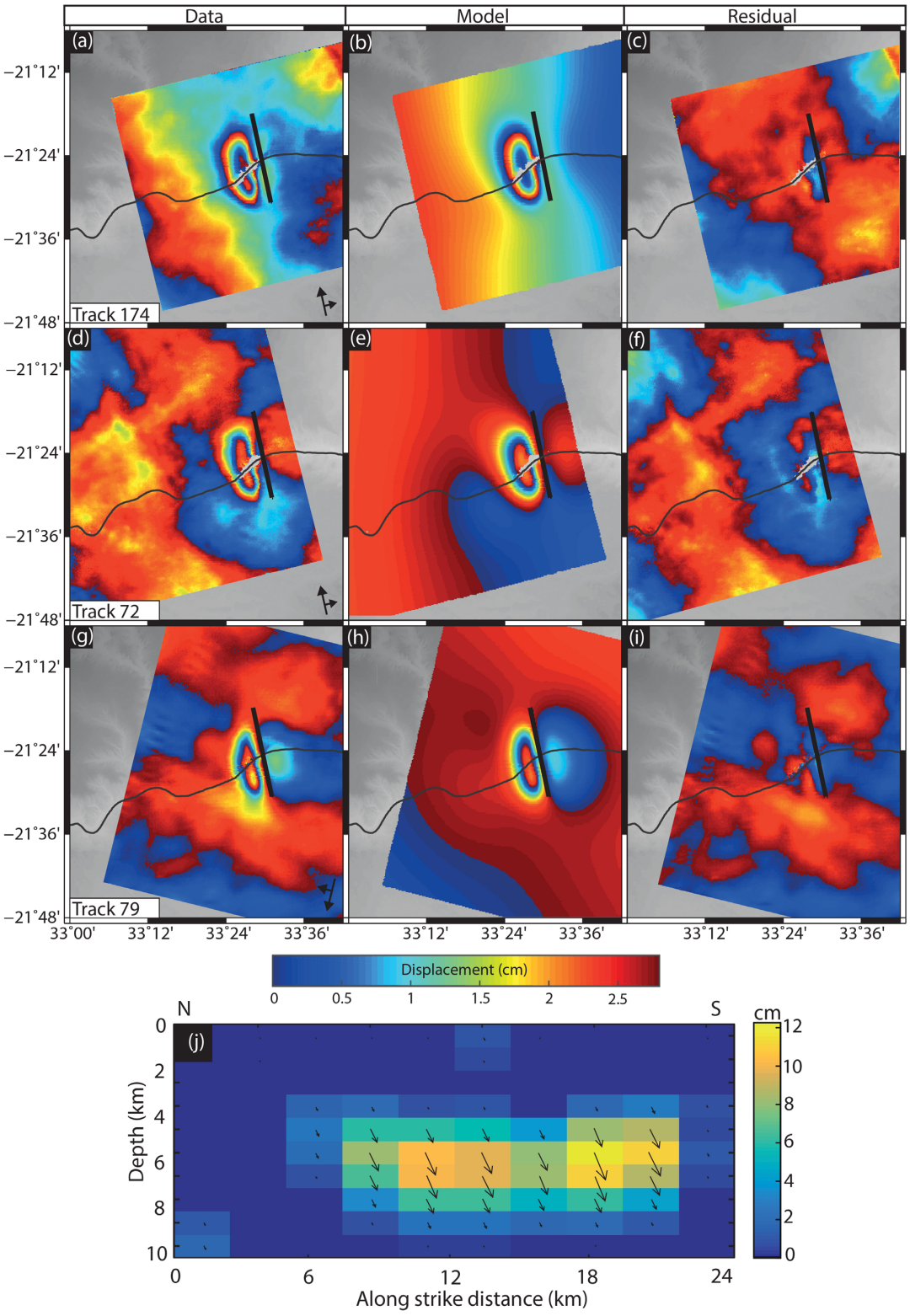

Figure A6. Fixed rake (−71°) model for the Zinave earthquake. (a–c) Data, model and residual to the distributed slip model for track 174. (d–f) Track 72 data, model and residual. (g–i) Track 79 data, model and residual. The black lines though (a–i) mark the top of the distributed slip model, where it intersects the surface. (j) Distributed slip model result for the inversion of tracks 174, 79 and 72 with rake fixed to −71°. The arrows show displacement of the east block relative to west (i.e. motion to the south is left-lateral).

Downloaded from https://academic.oup.com/gji/article-abstract/217/1/504/5298869 by University of Bristol Library user on 07 March 2019

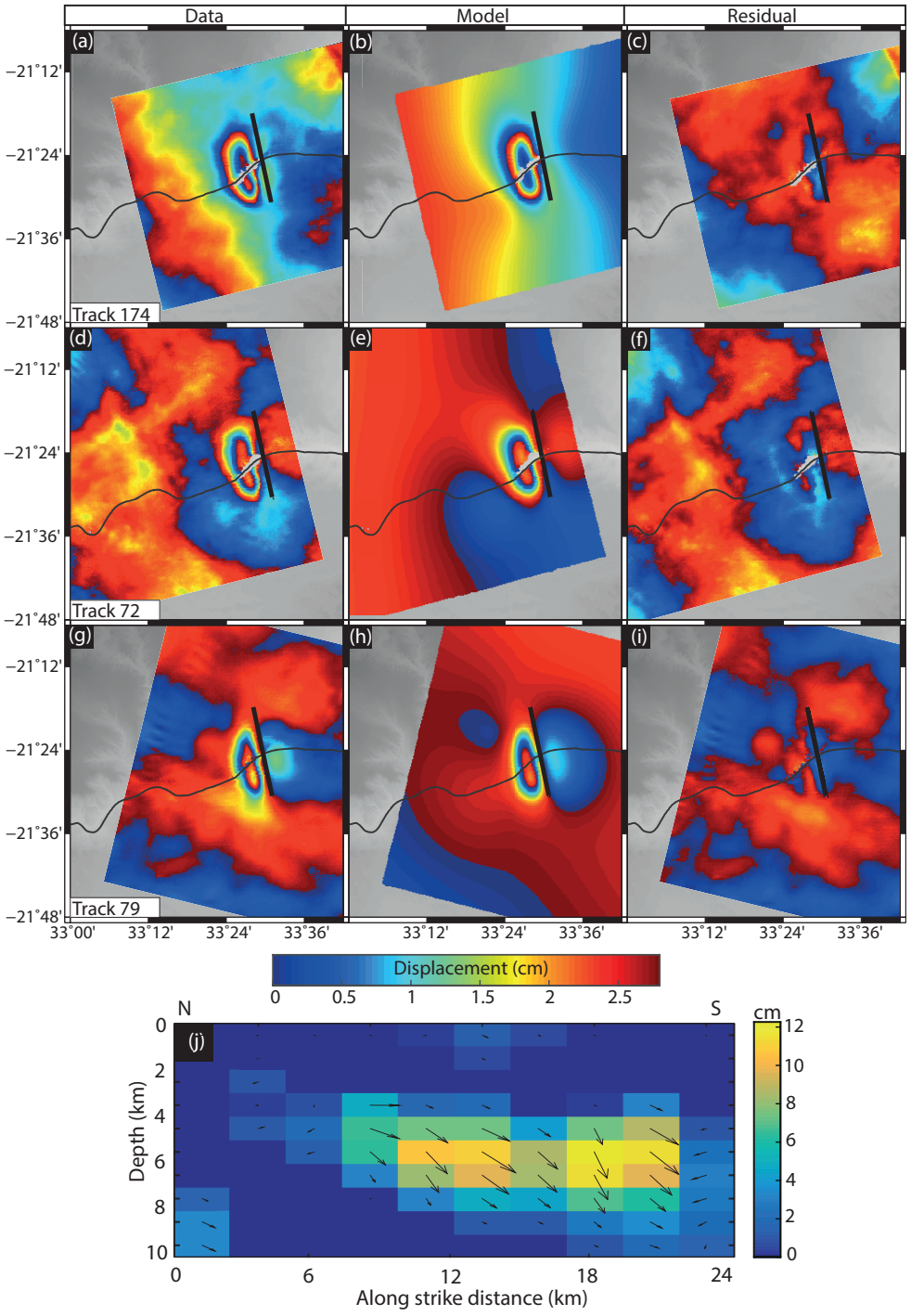

Figure A7. Variable rake model for the Zinave earthquake. (a–c) Data, model and residual to the distributed slip model for track 174. (d–f) Track 72 data, model and residual. (g–i) Track 79 data, model and residual. The black lines though a–i mark the top of the distributed slip model, where it intersects the surface. (j) Distributed slip model result for the inversion of tracks 174, 79 and 72 with variable rake. The arrows show displacement of the east block relative to west (i.e. motion to the south is left-lateral).

Downloaded from https://academic.oup.com/gji/article-abstract/217/1/504/5298869 by University of Bristol Library user on 07 March 2019

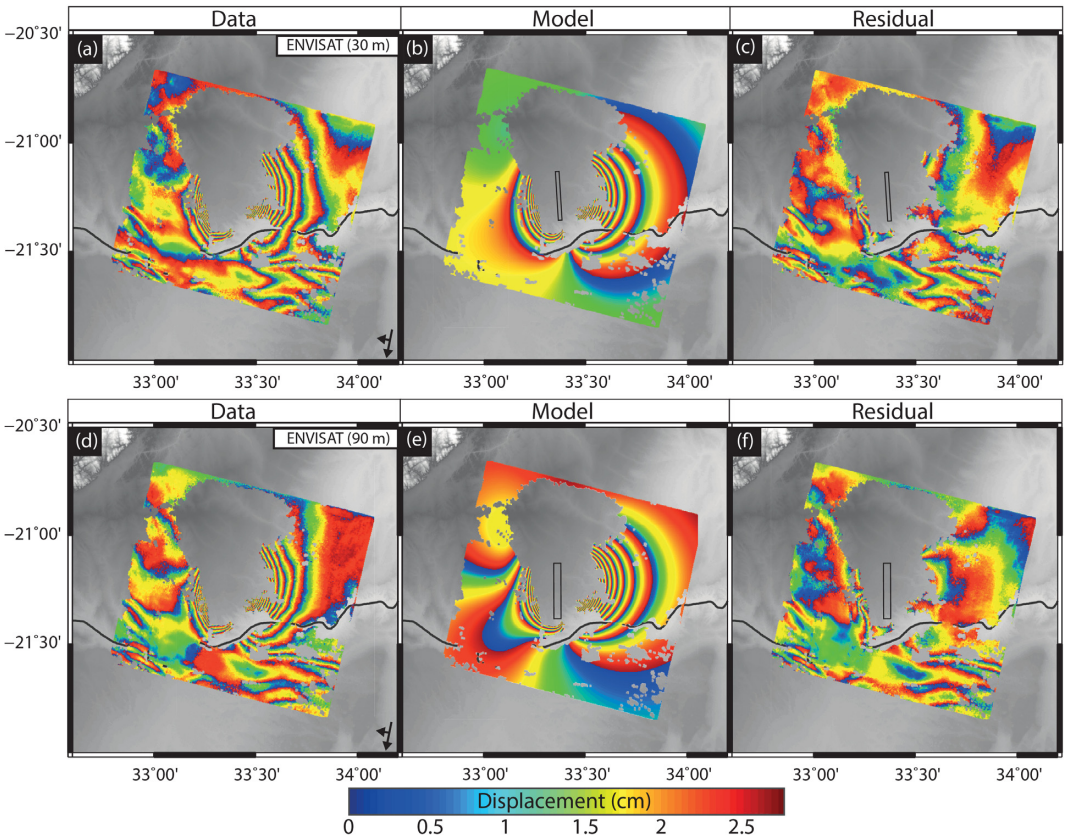

Figure A8. (a) Data, (b) model and (c) residual for the uniform slip model of the Machaze earthquake, using ENVISAT data at 30 m resolution. (d) Data, (e) model and (f) residual for the uniform slip model of the Machaze earthquake, using ENVISAT data resampled to 90 m. Root-mean-square misfit values can be found in Tables 1 and A3.

Downloaded from https://academic.oup.com/gji/article-abstract/217/1/504/5298869 by University of Bristol Library user on 07 March 2019

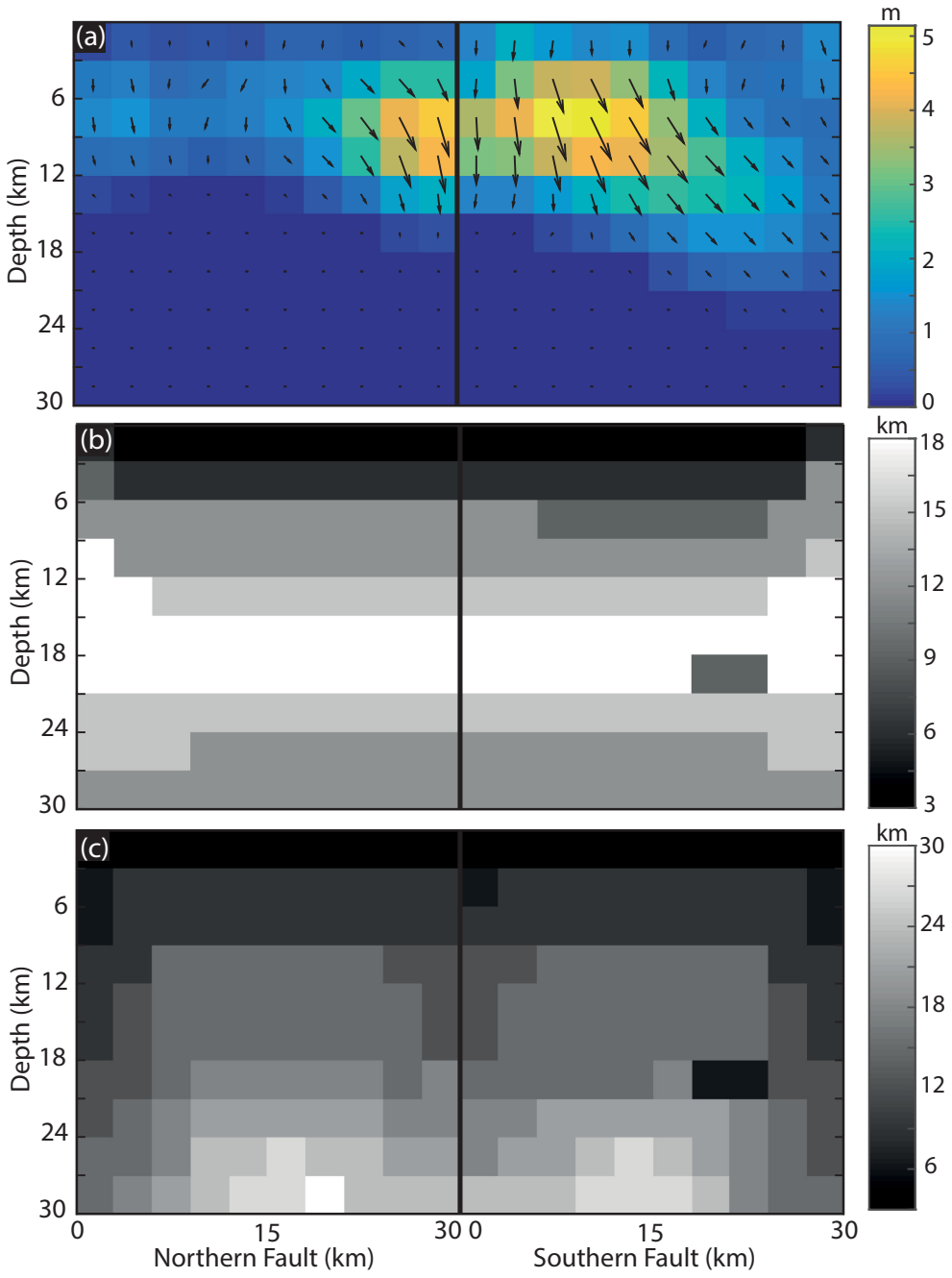

Figure A9. (a) Slip distribution for the Machaze earthquake using ENVISAT and SPOT data. (b) Length scale of vertical resolution. (c) Length scale of horizontal resolution. Each cell is 3 km horizontally by 3 km vertically.

Downloaded from https://academic.oup.com/gji/article-abstract/217/1/504/5298869 by University of Bristol Library user on 07 March 2019

Table A1. Summary of Sentinel-1 InSAR data used in this study. Line-of-sight vector is given as east, north, up.

Satellite	Track	Pass direction	Line-of-sight vector (E, N, U)	Number of interferograms	Coseismic interferograms	Stacked
Sentinel-1	79	Desc	0.5446 −0.1334 0.8280	19	7	4
	–	–	–	–	–	13/08/2017–06/10/2017
	–	–	–	–	–	13/08/2017–30/10/2017
	–	–	–	–	–	06/09/2017–06/10/2017
	–	–	–	–	–	06/09/2017–30/10/2017
	174	Asc	−0.5251 −0.1262 0.8416	35	14	6
	–	–	–	–	–	23/07/2017–29/09/2017
	–	–	–	–	–	23/07/2017–11/10/2017
	–	–	–	–	–	12/08/2017–11/10/2017
	–	–	–	–	–	12/08/2017–04/11/2017
	–	–	–	–	–	17/09/2017–29/09/2017
	–	–	–	–	–	17/09/2017–04/11/2017
	72	Asc	−0.6848 −0.1755 0.7073	25	13	6
	–	–	–	–	–	19/08/2017–24/09/2017
	–	–	–	–	–	19/08/2017–18/10/2017
	–	–	–	–	–	31/08/2017–18/10/2017
	–	–	–	–	–	31/08/2017–30/10/2017
	–	–	–	–	–	12/09/2017–24/09/2017
	–	–	–	–	–	12/09/2017–30/10/2017

Table A2. Initial conditions and inversion bounds for each parameter for the uniform slip distribution inversion of the Zinave and Machaze earthquakes.

Uniform slip bounds		Zinave	Machaze
Length (km)	Lower	8	5
	Initial	15	60
	Upper	25	100
Width (km)	Lower	0.5	1
	Initial	4	15
	Upper	10	35
Depth (km)	Lower	0.5	0.2
	Initial	6	10
	Upper	15	40
Dip (°)	Lower	−85	0.01
	Initial	70	70
	Upper	85	89.9
Strike (°)	Lower	Variable	140
	Initial	(see the text)	196
	Upper	–	280
X (km)	Lower	−8	−25
	Initial	0	0
	Upper	8	25
Y (km)	Lower	−8	−25
	Initial	0	0
	Upper	8	25
Strike-slip (m)	Lower	−0.4	−3
	Initial	0	0
	Upper	0.4	5
Dip slip (m)	Lower	−1	−6
	Initial	0	0
	Upper	0	10

Downloaded from https://academic.oup.com/gji/article-abstract/217/1/504/5298869 by University of Bristol Library user on 07 March 2019

Table A3. Fault parameters from the geodetic inversions, with 95 per cent confidence, and USGS focal mechanism for comparison. Fault locations (X and Y, UTM) in the geodetic inversions are for the middle of the bottom of the fault. Root-mean-square (rms) misfit is the joint rms if more than one data set is used in the inversion.

	USGS solution		T174		T72		T79		T174 + T72		T174 + T72 + T79	
Inversion points	–		695		743		633		1438		2071	
	FP1	FP2	Optimal	95 per cent range	Optimal	95 per cent range	Optimal	95 per cent range	Optimal	95 per cent range	Optimal	95 per cent range
Length (m)	–	–	16 700	13 500–19 300	16 300	14 600–17 900	15 600	14 600–17 000	16 000	14 800–17 600	15 800	14 900–16 800
Width (m)	–	–	5800	700–7400	1600	700–3300	4800	1600– 6700	35 000	700–3500	5100	1400–5700
Depth (m)	15 500	15 500	8400	5100–9800	5200	4500–6300	7300	5600–8700	6500	4800–6600	7600	5600–8100
Dip (°)	45	50	61	47–79	72	59–78	60	52–67	65	60–76	59	54–68
Strike (°)	334	185	168	163–173	169	166–171	168	166–170	169	166–171	168	167–170
X (m)	550 800	550 800	546 100	545 000–549 000	548 700	547 600–549 100	546 700	545 600–548 300	547 600	547400–548 900	546 600	545 900–548 400
Y (m)	7 630 800	7 630 800	7 629 900	7 628 200–763 200	7 629 400	7 628 600–7 630 700	7 631 000	7 629 700–7 632 300	7 629 400	7 628 800–7 630 600	7 629 300	762 900–7 632 200
Strike-slip (m)	–	–	0.05	−0.33–0.37	0.31	0.08–0.39	−0.11	−0.32–0.00	0.12	0.07–0.39	0.06	0.0– 0.20
Dip slip (m)	–	–	−0.14	−0.93—0.12	−0.32	−0.83– −0.17	−0.12	−0.35—0.09	−0.17	−0.77—0.17	−0.14	−0.47– −0.12
Rake (°)	−114	−68	−72	–	−46	–	47	–	−55	–	−66	–
rms (cm)	–		0.8	–	0.5	–	0.5	–	1.0	–	1.0	–

Downloaded from https://academic.oup.com/gji/article-abstract/217/1/504/5298869 by University of Bristol Library user on 07 March 2019

Table A4. Root-mean-square (rms) residuals for the variable rake, uniform slip rake (−66°) and body wave slip rake (−71°), with associated F-statistic values.

rms (cm)	Variable rake	Uniform slip rake	Body wave rake
Joint	0.44	0.44	0.44
Track 174	0.47	0.47	0.47
Track 79	0.43	0.43	0.43
Track 72	0.43	0.43	0.43
F-statistic	–	0.0045	0.0045

Downloaded from https://academic.oup.com/gji/article-abstract/217/1/504/5298869 by University of Bristol Library user on 07 March 2019